Wang *et al. eLight* (2025) 5:8
https://doi.org/10.1186/s43593-025-00082-0

elight.springeropen.com

RESEARCH ARTICLE **Open Access**

Free-space terabit/s coherent optical links via platicon frequency microcombs

Wenting Wang[1,2*†], Hao Liu[1†], Jiagui Wu[1†], James F. McMillan[1†], Dong IL Lee[1*], Futai Hu[1], Wenzheng Liu[1], Jinghui Yang[1], Hangbo Yang[1], Abhinav Kumar Vinod[1], Yahya H. Ezzeldin[3], Christina Fragouli[3], Mingbin Yu[4,5], Patrick Guo-Qiang Lo[4,6], Dim-Lee Kwong[4], Devin S. Kahrs[7], Ninghua Zhu[8] and Chee Wei Wong[1*]

Abstract

Coherent frequency microcombs, generated in nonlinear high-Q microresonators and driven by a single continuous-wave laser, have enabled several scientific breakthroughs in the past decade, thanks to their high intrinsic phase coherence and individual comb line powers. Here, we report terabit-per-second-scale coherent data communications over a free-space atmospheric link, using a platicon frequency microcomb, employing wavelength- and polarization-division multiplexing for next-generation optical wireless networks. Spanning more than 55 optical carriers with 115 GHz channel spacing, we report the first free-space coherent communication link using a frequency microcomb, achieving up to 8.21 Tbit/s aggregate data transmission at a 20 Gbaud symbol rate per carrier over 160 m, even under log-normal turbulent conditions. Utilizing 16-state quadrature amplitude modulation, we demonstrate retrieved constellation maps across the broad microcomb spectrum, achieving bit-error rates below both hard- and soft-decision thresholds for forward-error correction. Next, we examine a wavelength-division multiplexing free-space passive optical network as a baseline for free-space fronthaul, achieving an aggregate data rate of up to 5.21 Tbit/s and a field-tested spectral efficiency of 1.29 bit/s/Hz in the microcomb-based atmospheric link. We also quantify experimental power penalties of ≈ 3.8 dB at the error-correction threshold, relative to the theoretical additive white Gaussian noise limit. Furthermore, we introduce the first-ever demonstration of master–slave free-space carrier phase retrieval with frequency microcombs, and the compensation for turbulence-induced intensity scintillation and pointing error fluctuations, to improve end-to-end symbol error rates. This work provides a foundational platform for broadband vertical heterogeneous connectivity, terrestrial backbone links, and ground-satellite communication.

Keywords Frequency microcombs, Terabit/s data rate, Free-space optical link, Coherent wireless fronthaul

---

[†] Wenting Wang, Hao Liu, Jiagui Wu and James F. McMillan have contributed equally to this work.

*Correspondence:
Wenting Wang
wentingwang@ucla.edu
Dong IL Lee
dilee@ucla.edu
Chee Wei Wong
cheewei.wong@ucla.edu
[1] Fang Lu Mesoscopic Optics and Quantum Electronics Laboratory, University of California, Los Angeles, CA 90095, USA
[2] Present Address: Mesoscopic Optics and Advanced Instruments Laboratory, School of Optics and Photonics, Beijing Institute of Technology, Beijing, China
[3] Algorithmic Research in Network Information, University of California, Los Angeles, CA 90095, USA
[4] Institute of Microelectronics, a*STAR, Singapore 117865, Singapore
[5] State Key Laboratory of Functional Materials for Informatics, Shanghai Institute of Microsystem and Information Technology, Shanghai, China
[6] Advanced Micro Foundry, Singapore 117685, Singapore
[7] Tektronix, Santa Clara, CA 95054, USA
[8] Institute of Intelligent Photonics, NanKai University, Tianjin, China

1 Introduction

With the advent of wavelength-division multiplexing (WDM), fiber-based long-haul communications have experienced significant advancements, leading to dramatic improvements in land-based communication bandwidths and network topologies for terrestrial systems. Emerging communication-related optoelectronic components and photonic integrated circuits have significantly advanced optical transceivers by integrating narrow-linewidth lasers [1], optical waveguide amplifiers [2], frequency microcombs [3–5], and high-speed, high-responsivity photodetectors [6], along with heterogeneous technology [7] to enhance performance and integration while ultra-wideband modulators [8] improve data efficiency. These developments have facilitated the increasing demands for high-speed data across diverse fields such as telecommunications, energy-efficient interconnects, high-definition remote conferencing, virtual environments, healthcare, large-scale computing, and high-energy particle physics experiments [9–13]. However, this growth has led to congestion in the last-mile wireless access networks within the allocated GHz radio frequency (RF) spectrum. This has prompted a shift toward using higher-frequency and optical carriers for wireless communications [14–16]. A range of advantages of optical wireless communication (OWC) includes access to THz-level bandwidth, unrestricted spectrum usage, easy of deployment, smaller and lighter receivers, and enhanced channel security. In 5G and beyond 5G networks, the integration of networked flying platforms—such as unmanned aerial vehicles, drones, and high-altitude balloons—has emerged as a promising approach to expanding network coverage and capacity. These platforms serve as wireless fronthaul/backhaul links in space-air-ground-sea integrated networks, leveraging hybrid millimeter-wave and free-space optical (FSO) links to further enhance connectivity. Moreover, FSO communication is being increasingly used for both terrestrial and satellite links [17–20], enabling building-scale relay networks, backbone links, and three-dimensional geostationary satellite networks for global broadband coverage [21]. Recent trials have demonstrated remarkable Tb/s FSO transmission using multi-laser arrays for wavelength-division multiplexing. These systems incorporate programmable wavelength-selectable switches to equalize intensity across the array and employ electronic control units for double-pass building-to-building links [22, 23]. Significant progress has also been made with coherent detection techniques [24], co-transmitted local oscillator tones in Kramers–Kronig schemes [25], and spatial-mode multiplexing [24, 26], all contributing to further advancements in free-space data transmission.

In parallel, microresonator-based frequency combs have emerged as a transformative chip-scale platform [27–34], offering unique spectral properties that revolutionize a range of applications, including mode-locked oscillators [35], precision frequency metrology [36, 37], astrophysical spectrographs [38, 39], laser spectroscopy [40–42], distance ranging [43–46], coherent microwave and sub-millimeter wave generation [47–53], and convolutional processing networks [54, 55]. Frequency microcombs, in particular, have shown great promise for enabling massively parallel data transmission. These combs, generated from phase-locked discrete channels within a single source, allow for high data rates with significantly reduced size, weight, and power (SWaP) requirements. Demonstrations of soliton microcombs [56, 57], dark pulse microcombs [58], and high-data modulation formats [59] in fiber-based links have highlighted their potential for large-capacity transmission. The phase coherence of frequency microcombs simplifies error correction, as the highly correlated phase and intensity fluctuations between comb lines reduce computational complexity and inter-channel guard bands [60, 61]. Notably, the Kerr soliton microcomb has enabled terabit-scale data transmission over long fiber links, with two-point locking and pump laser conveyance playing key roles [62]. This coherence also facilitates high-capacity digital-analog wireless fronthaul with advanced modulation formats [10]. Recent work has demonstrated the use of dual-interleaved soliton microcombs and combined wavelength- and polarization-multiplexing techniques to achieve aggregate data rates up to 55 Tb/s across 179 carriers in fiber [56]. Further, spatial-mode multiplexing and higher-order digital modulation have yielded net data rates of 1.84 Pbit/s with 223 wavelength-multiplexed channels [63], and a spectral efficiency of 10.4 bits/s/Hz in fiber-based testbeds [59]. Using various orthogonal multiplexing schemes, data rates up to 49.7 Tb/s per fiber core have been realized with frequency microcombs [62], with even higher rates (97.7 Tb/s) demonstrated using bulk laser combs [64]. These developments have been further complemented by advances in on-chip scalable terabit data transmitters, utilizing mode-division multiplexers, multimode couplers, chip-scale interleavers, microring modulators, dispersion compensation, and spectral filters on silicon photonic circuits, enabling efficient data-center interconnections [9, 65–67]. Super-broadband on-chip continuous spectral translation has also been used to enable coherent data transmission at targeted wavelengths [68]. In addition to fiber-based communications, FSO communication has recently been demonstrated using soliton microcombs with pulse position modulation [69] and differential phase-shift keying [70].

Here, we present the first demonstration of terabit-scale coherent data transmission in a free-space atmospheric link, utilizing an intensity-equalized platicon frequency microcomb. By exploiting over 55 optical carriers in both wavelength- and polarization-multiplexed subspaces, we achieve an aggregate data rate of 8.21 Tbit/s, with a 20 Gbaud symbol rate per carrier, 115 GHz channel spacing, and a transmission distance of over 160 m (including both indoor and outdoor hybrid links), even under log-normal turbulent conditions. We explore 16-state quadrature amplitude modulation (QAM), characterizing the retrieved constellation maps line-by-line across the efficient platicon microcomb, and demonstrating that the free-space communication bit-error rates (BER) remain below the hard- and soft-decision thresholds for forward error correction (FEC). Next, we demonstrate wavelength division multiplexing in a free-space passive optical network (PON) fronthaul, reducing raw error rates to 6.5×10^{-5} over 10^6 symbols while maintaining the signal quality. Using advanced digital signal processing (DSP) algorithms and accounting for FEC overheads, we report an aggregate data rate of 5.21 Tbit/s in our single-wavelength free-space fronthaul, achieving a spectral efficiency of 1.3 bit/s/Hz and a 3.8 dB power penalty compared to the theoretical additive white Gaussian noise (AWGN) limit. Finally, in our platicon microcomb free-space testbed, we quantify the impact of turbulence-induced intensity scintillation and pointing error fluctuations on end-to-end symbol error rates. We also present, for the first time, a master–slave free-space carrier phase retrieval technique using frequency microcombs.

2 Results

2.1 Microresonator-based platicon frequency microcomb generation

A conceptual wireless optical communication scenario for a line-of-sight atmospheric link in wireless networks is depicted in Fig. 1a. Inset **i** shows the optical micrograph of the microresonator used for platicon frequency microcomb generation, while inset **ii** illustrates the free-space WDM-PDM coherent optical communication system. Multiple comb lines are utilized as optical carriers for data transmission, leveraging a unique dual-polarization in-phase and quadrature-phase modulator for polarization multiplexing. We utilized the different modulation methods shown in inset **iii** and **iv**. To ensure broadband operation, we implement a normal dispersion microresonator frequency comb, which features a platicon spectral generation that minimizes the intensity variation of the comb lines to less than 19 dB over a 12.5 THz (100 nm) bandwidth, as shown in Fig. 1b. Compared to soliton microcombs, Platicon microcombs offer higher pump power conversion efficiency, better comb profile uniformity and stability, and ease of operation [71]. The silicon nitride microresonator, designed with a $2\times0.8\ \mu\text{m}^2$ waveguide cross-section and a 200 μm radius, generates a transverse-magnetic (TM) polarized platicon microcomb when pumped by an amplified L-band tunable external cavity diode laser (ECDL). The generation process is initiated by modulation instability and four-photon processes (detailed in the Methods section). Prior to the microresonator, a narrow-bandwidth optical filter blocks the pump amplified spontaneous emission (ASE) noise, with residual ASE noise being superimposed on the microcomb lines as additive white Gaussian noise. We tune the

(See figure on next page.)

Fig. 1 Free-space optical (FSO) wireless coherent communications with an atmospheric horizontal link using a platicon frequency microcomb. **a** Conceptual illustration of a free-space line-of-sight optical wireless network based on a platicon frequency microcomb utilizing optical beams transmitted through the atmosphere to establish direct high-capacity communication links. Inset **i**: Optical micrograph of the microresonator used for platicon frequency microcomb generation illustrating the nanostructured device. The scale bar indicates a size of 200 μm. Inset **ii**: Diagram of the free-space Wavelength Division Multiplexing (WDM) and Polarization Division Multiplexing (PDM) coherent optical communication system. This setup incorporates four independent 50 GSa/s arbitrary waveform generators (AWGs) to drive the modulators. Key components include the dual-Polarization in-phase and quadrature Modulator (DP-IQ mod.), erbium-Doped fiber amplifier (EDFA) for signal modulation and amplification, and a coherent receiver (Coh. rec.) for detecting and processing the received signal. Inset **iii**: Conceptual illustration comparing the modulation schemes of previous systems versus our current approach using four independent AWGs with decorrelated data streams for In-phase and Quadrature polarization multiplexing. Inset **iv**: Side-by-side comparison of previous polarization multiplexing techniques versus the new methodology applied in this study. Prior scheme requires variable optical attenuators (VOA), delay line (DL), and polarization beam combiner (PBC) to simulate the polarization multiplexing. **b** Measured spectrum of the platicon frequency microcomb at an optical spectral resolution bandwidth (ORBW) of 50 pm, showcasing the distinct comb lines generated. The orange envelope represents the theoretical spectrum modeled using the Lugiato-Lefever equation.**c** Modeled temporal pulse duration of the platicon frequency microcomb, demonstrating a 1.7 ps Full Width at Half Maximum (FWHM) pulse duration. **d** Measured heterodyne Radio Frequency (RF) beat note between a comb line extracted from the platicon frequency microcomb and an external reference laser. This measurement supports the low-noise performance of the microcomb, confirming the coherence and stability of the frequency comb necessary for FSO communications. **e** Comparative analysis of leading fiber and free-space communication links, contrasting the performance of bulk laser frequency combs, distributed feedback (DFB) laser arrays, and frequency microcombs as optical transmitters. The analysis focuses on the Baud rates achieved in each system, with rates ranging from 24 to 35 Gbaud, highlighting the potential of frequency microcombs for higher data rates and bandwidth efficiency in FSO systems

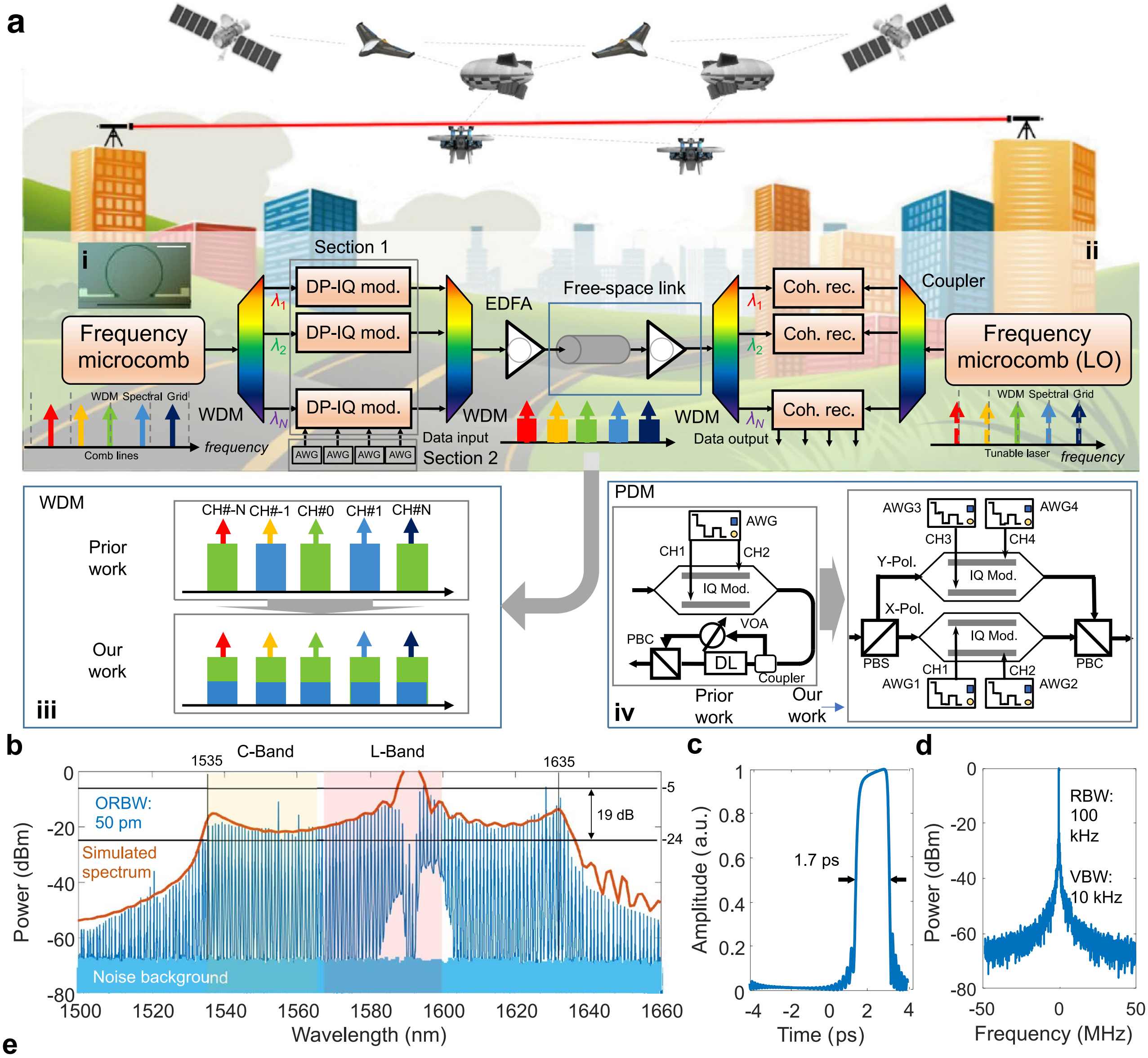

e

	Aggregate measured data rate (Tbit/s)	20-dB optical bandwidth	BER	Multiplex	Transmission	Power efficiency (Transceiver)
Fiber link: bulk laser comb [64]	97.7/core	100 nm	2.7×10^{-2}	WDM,PDM,SDM	Fiber: 31 km	High
Fiber link: microcomb [63]	49.7/core	90 nm	1.0×10^{-5} (LDPC)	WDM,PDM,SDM	Fiber: 7.9 km	Low
Free-space link: DFB 54 laser array [22]	13.16	22 nm	1.0×10^{-2}	DWDM,PDM	Vertical free-space (α_{vert}): 10.5 km	High
Free-space link: microcomb (this work)	8.21	100 nm	3.7×10^{-3}	WDM,PDM	Horizontal free-space (α_{hori}): 160 m	Low

Fig. 1 (See legend on previous page.)

pump wavelength from the blue-detuned side toward the pump resonance, resulting in a close-rectangular-shaped microcomb spectrum, as shown in Fig. 1b, with a conversion efficiency $\eta \approx 11\%$. The spectral roll-off factors for the long- and short-wavelength comb edges are 7.4 dB/nm and 3.0 dB/nm, respectively. This platicon microcomb provides over 100 high-quality optical carriers with an optical carrier-to-noise ratio (OCNR) of ≈ 50 dB, and the pre-amplified average power per comb line is ≈ 20 μW, derived from a total microcomb power of ≈ 2 mW. Slightly over 100 microcomb lines are generated in the C- and L-bands. The pre-amplified power per comb line is also shown in Fig. 1b. Subsequently, we employ a single-stage amplification with ≈ 20 dB gain, leading to ≈ 2 mW of power per comb line post-amplification. The microcomb source has a channel spacing of 115 GHz for continuous stable operation without significant power drift and dropping the low-noise comb state. The input platicon microcomb is modulated using polarization-diverse IQ modulators with four independent 50 GSa/s arbitrary waveform generators (AWGs), as shown in inset (ii) of Fig. 1a. Figure 1c illustrates the modeled pulse duration of 1.7 ps, derived from the rectangular comb spectral envelope. Intensity fluctuations and linewidth broadening are assessed using continuous-wave heterodyne beat-note measurements, shown in Fig. 1d, which involve individual comb lines and a standalone narrow linewidth (≈ 100 kHz) ECDL. These measurements confirm the low-noise performance of the comb, supporting its use in free-space coherent communications. The optical carriers, with high OCNR and narrow linewidth, are well-suited for high-capacity data transmission in coherent communication systems. Finally, a comparison of the free-space microcomb link parameters with those of fiber-based laser frequency comb links is provided in Fig. 1e. The state-of-the-art performance of a commercial 54-laser array free-space link is also highlighted.

2.2 Free-space PDM-WDM coherent data transmission

Figure 2a illustrates the setup for free-space PDM-WDM coherent data transmission over a 160 m horizontal atmospheric link, based on our platicon frequency microcomb. The microcomb is spectrally split into the C- and L-bands using a fiber-based WDM, followed by independent amplification of each spectral band via C- and L-band amplifiers to boost the average optical power. The optical carrier microcomb consists of 28 C-band and 27 L-band carriers, which are injected into polarization-multiplexed IQ modulators. The aerial view inset **i** of Fig. 2a shows the field trial setup for the free-space link. Detailed design and stabilization of the link are described in Supplementary Information Sections III and IV. To compensate for insertion and modulation losses, Fig. 2b shows the raw output spectra for both the C-band (with ≤ 4 dB power variation and ≥ 30 dB optical signal-to-noise ratio, $\mathrm{OSNR_{TX}}$) and L-band (with ≤ 6 dB power variation and ≥ 28 dB $\mathrm{OSNR_{TX}}$, excluding the adjacent pump wavelength region). The L-band spectrum exhibits lower OSNR near the 1591 nm pump wavelength due to residual pump ASE noise. $\mathrm{OSNR_{TX}}$ is defined as the optical signal-to-noise ratio at the transmitter, considering the optical carrier-to-noise ratio (OCNR) and ASE noise from the first C/L band erbium-doped fiber amplifiers (CEDFA1/LEDFA1) before the free-space link. The platicon comb transmitter subsystem achieves an average $\mathrm{OSNR_{TX}} \approx 30$ dB over the 55 C- and L-band carriers, enabling the link.

To maximize spectral efficiency, we implement PM-16QAM to encode the data stream onto each frequency microcomb channel at a 20 Gbaud symbol rate. The PDM IQ modulators are driven by four independent high-performance AWGs, as detailed in Supplementary Information Section II and summarized in the Methods. These AWGs generate four uncorrelated, timing-synchronized pseudo-random bit sequences (PRBS) to drive the in-phase and quadrature-phase arms at the X- and Y-polarizations (termed XI, XQ, YI, YQ), eliminating the need for additional time delays to uncorrelate the data streams. Digital pre-compensation is performed to mitigate the non-idealities of the modulator, AWG, and coherent receiver frequency response. Additionally, a PDM-WDM system

(See figure on next page.)

Fig. 2 Coherent PDM-WDM data transmission over a 160 m horizontal point-to-point free-space link. **a** The experimental setup of a free-space optical PDM-WDM communication system. The setup involves multiple wavelengths and polarizations being transmitted over the link to achieve high data throughput. Inset **i**: Aerial map illustrating the layout of the free-space link field trial. This map shows the horizontal point-to-point optical communication setup and highlights key locations such as the transmitter, receiver, and line-of-sight path. Inset **ii**: Schematic diagram of the beam expander/reducer used in the optical system. **b** Measured optical spectrum showing all C-band and L-band channels, with a resolution of 100 pm ORBW. This spectrum highlights the wavelength range used for the transmission and demonstrates the effectiveness of WDM in leveraging multiple channels for high-capacity data communication. **c** Example retrieved constellation diagrams of representative C-band channels for both XY polarizations. The Error Vector Magnitude (EVM) values corresponding to each channel indicate the degree of signal distortion, with lower EVM values reflecting better signal integrity. The measured constellation points are not elongated along the azimuthal direction, indicating minimal phase noise and strong signal coherence during transmission. **d** Measured Bit Error Rates (BERs) for each data channel across the C- and L-bands for both the free-space link (denoted by white squares) and the back-to-back interconnect (denoted by blue triangles). The error bars represent the standard deviation, providing an indication of the measurement's reliability. The BER thresholds are set at 4.5×10^{-3} for hard-decision Forward Error Correction (FEC) and 1.5×10^{-2} for soft-decision FEC, with respective overheads of 7% and 20%. The purple dashed box on the left highlights the EDFA noise region, where the transmitter optical carrier signal to noise ratio (SNR) is lower due to amplification noise constraints. The light blue dashed-box region marks areas with environmental variations, such as pointing errors, which can affect the transmission quality during the measurement set. **e** Example retrieved constellation diagrams for representative L-band PDM-WDM data transmission

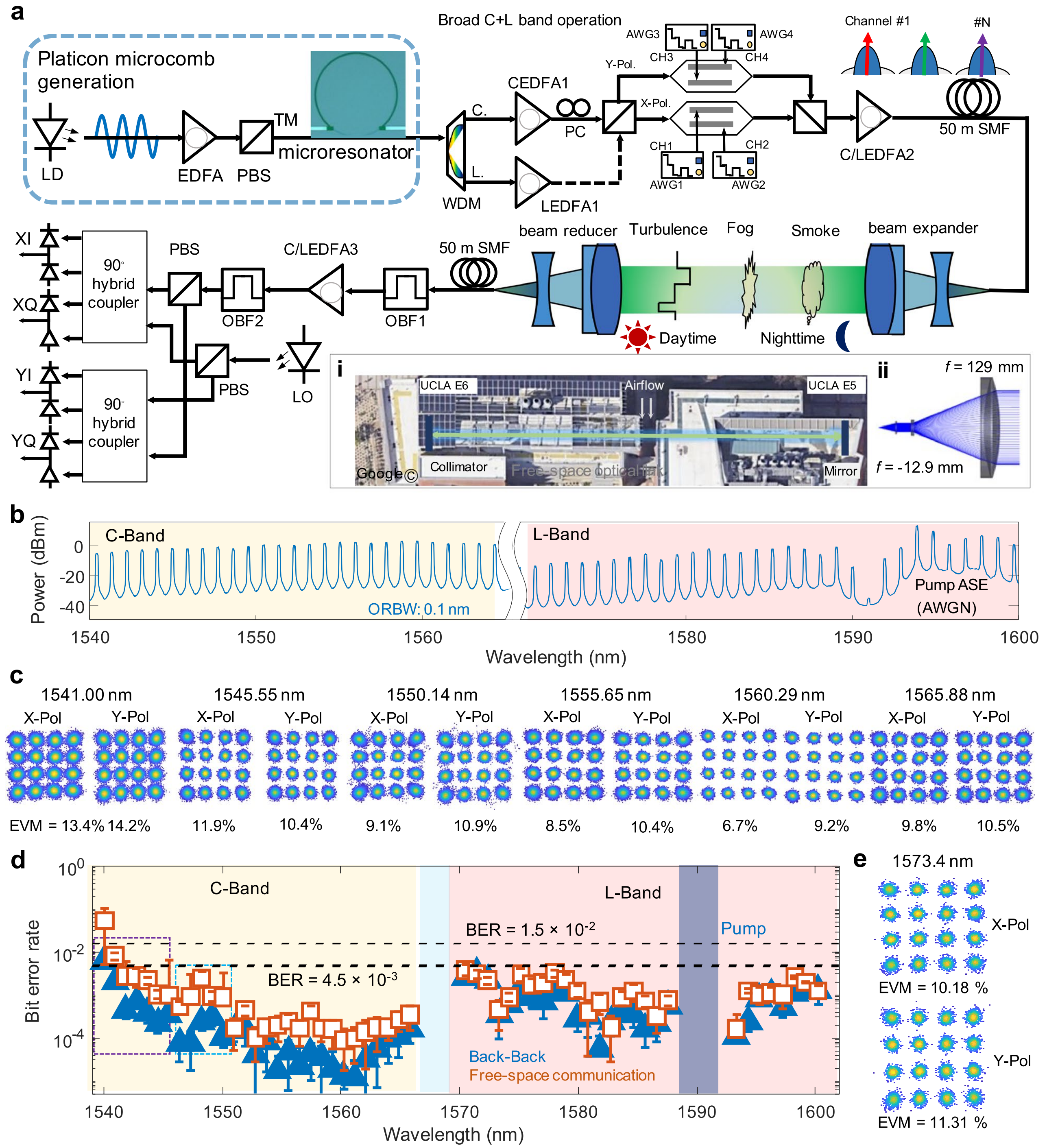

Fig. 2 (See legend on previous page.)

simulation is conducted to analyze adjacent channel crosstalk with a channel spacing of 115 GHz, emulating a practical WDM system. In the free-space link between two buildings at UCLA, the transmitted optical signal at 200 mW (through a second set of C/L amplifiers, C/L EDFA2) is first beam-expanded into a 40 mm diameter beam using a 10× beam expander (Fig. 2a inset **ii**). The beam is reflected from a 2-inch silver mirror located on the other building, after ensuring eye safety (≈ 0.004 W/cm^2 in our link, well below the IEC 60825 safety standards requirement of 4 W/cm^2). The received optical signal is coupled back through a 10× beam reducer into a 50-m single-mode fiber (negeligible coherence and SNR penalties), which connects to other fiber-based components while shielding out visible and ambient light from the system. Following the 160 m building-to-building atmospheric data transmission, a polarization-diverse dual-channel coherent receiver is employed to assess the transmission quality of each channel through a broadband tunable optical bandpass filter (OBPF) and a tunable ECDL.

To calibrate the polarization diversity, we first characterize the polarization response of the system using two independent ECDLs and binary phase modulation, extracting the system's polarization Jones matrix. A third set of C/L-band amplifiers (C/L EDFA3) compensates for the free-space link loss and suppresses coherent receiver shot noise. Two synchronized real-time oscilloscopes with four channels digitize the received electrical waveforms (XI, XQ, YI, YQ) for offline DSP. To enhance the platicon microcomb free-space link, DSP algorithms including matched filtering, IQ and XY-polarization time skew correction, offset frequency estimation, optical phase estimation, symbol decision, and demodulation mapping are employed (detailed in Methods and Supplementary Information Section II).

Figure 2c shows example received constellations along with the measured error vector magnitude (EVM) [72] for the C-band, with spectral steps of ≈ 4.5 to 5 nm for both polarizations, and an average power of 6.9 mW per channel (measured at the receiver after filtering out each platicon comb line and pre-amplification). Between the channels, after pre-amplification, the receiver power fluctuation is ≈ 1.8 dB. The deviation of the measured constellations from ideal points shows some anisotropy, which increases along the radial direction due to power fluctuations in the complex waveforms. The retrieved constellations are not elongated along the azimuthal direction, indicating no excessive phase noise. Notably, nonlinear impairments are avoided even with higher transmitted average power, and temporal walk-off from chromatic dispersion is negligible in the free-space optical channel. Intradyne reception is conducted to assess the communication quality. For optimal data transmission quality, the EDFA pump currents are optimized by continuously monitoring the BER and quality factors Q_{dB}^2 from the eye diagram. Both BER and EVM are used as quantitative metrics for data transmission quality. EVM quantifies the effective distance of the received symbols from their ideal positions in the constellation diagram, where the error vector follows a Gaussian-shaped joint probability density function centered at the respective constellation points. Due to minimal nonlinear and electronic noise in the subsystem, EVM is correlated with BER in the optical additive white Gaussian noise channel. After optimizing system parameters to minimize microcomb phase and intensity fluctuation effects, back-to-back data transmission is performed over the C- and L-band optical carriers.

Figure 2d illustrates the achieved free-space data transmission after optimizing the communication system and increasing the output power via the second amplifier pairs (C/L EDFA2). The increased transmitted average power compensates for geometric loss in the free-space link, especially over longer distances, and mitigates power impairments caused by turbulence-induced propagation beam spatial walk-off and wander, as well as acoustic variation-induced pointing errors (PE). The geometric loss is determined by the beam coupling loss, around 5 dB for our free-space optical channel. Figure 2d shows the achieved BER, comparing the decoded bit sequence with the transmitted sequence. All comb lines, except for the 1541.002 nm line, exhibit BERs below the thresholds of 1.5×10^{-2} and 4.5×10^{-3} (black dashed line), which are suitable for post-correction and error-free communication. After applying FEC with a 20% and 7% overhead, the post-FEC BER is reduced to below 10^{-15}, enabling error-free transmission over the 160 m free-space link. This allows an aggregate data rate of 8.21 Tbit/s and a spectral efficiency of 1.29 bits/s/Hz across the 28 C-band and 27 L-band channels, factoring in the BER threshold and FEC redundancy for each channel. Figure 2e shows representative constellation diagrams for the L-band at the 1573.4 nm channel, along with the corresponding EVM for both polarizations. Due to the large channel spacing, good frequency grid stability, and associated QAM pulse shaping and matched filtering, coherent inter-channel crosstalk is negligible in our link. Previous studies [73] have shown that an extinction ratio (ER) of over 22.2 ± 1.5 dB between adjacent channels is sufficient to suppress inter-channel crosstalk, aided by commercial tunable delay interferometers or programmable wave-shaping instruments. Our demonstrated free-space PDM-WDM coherent data transmission platform enables Tbit/s point-to-point wireless communications for short-reach distances. For longer reach distances, further enhancement of the OSNR will be required. Additionally, the WDM communication is demonstrated with a single transmitter, confirming the validity of coherent data demodulation for an uncorrelated data stream, and setting the stage for next single carrier PDM-FSO data transmission demonstrations.

2.3 Coherent wavelength-multiplexed free-space fronthaul with testbed parameters

Advancing from the PDM-WDM approach, the single carrier PDM-based free-space fronthaul data distribution offers enhanced noise tolerance by leveraging the high power of individual amplified comb lines, effectively overcoming the residual pump ASE noise in WDM-based free-space passive optical networks (WDM-FS-PONs). This technique assigns a unique wavelength to each optical network unit, providing a robust baseline testbed demonstration for high-rate, wavelength-multiplexed links and validating the coherent demodulation of temporally uncorrelated data streams using the developed DSP algorithms. Single-carrier data transmission, incorporating a longer symbol length and polarization diversity, is performed over the same free-space link. An individual optical carrier is selected after the first EDFA (CEDFA1/LEDFA1), with corresponding data demodulation performed on each to validate the DSP scheme. Details of the single-wavelength fronthaul link are provided in Supplementary Information Section II.

Due to the low occurrence of errors, we use the EVM metric instead of the BER to rigorously quantify data transmission quality. Figure 3a presents the EVM distribution for 35 individual carriers in the frequency comb L-band, along with a 16-QAM EVM threshold of 12.5% for post-correction error-free transmission, as indicated by the dashed black line. The EVM for dual polarization (X and Y) remains below the threshold for all channels except for the suppressed pump channel. Fluctuations in the EVM for wavelengths above 1586 nm are attributed to varying OSNR, as detailed in Supplementary Information Section II. Over the 35 independent wavelength channels in the 160 m atmospheric free-space access link, an aggregated data rate of up to 5.6 Tbit/s is anticipated. Including a 7% overhead, the potential aggregated total data rate is estimated at 5.21 Tbit/s, with a spectral efficiency of 1.29 bits/s/Hz. This demonstrates a solution for free-space wavelength-multiplexed high-rate access networks.

Figure 3b compares the performance of our platicon comb-based transceiver against state-of-the-art ECDLs, as well as the theoretical BER limit determined by AWGN. This comparison is made for three arbitrary wavelengths (1542.93, 1552.96, and 1561.32 nm) during back-to-back data transmission. The OSNR is attenuated in 1.5 dB steps from 27 to 12 dB, increasing the ASE noise loading ratio, as explained in Methods and Supplementary Information Section II. At the hard-decision FEC BER threshold of 4.5×10^{-3}, the comb-based transceiver incurs an $\approx$ 3.8 dB OSNR degradation (power penalty) relative to the theoretical white noise BER limit for 16-QAM, while the ECDL-based transceiver shows a 3.3 dB degradation. The additional 0.5 dB OSNR degradation from the platicon microcomb is attributed to the additive ASE noise from the first EDFA. This examination affirms the viability of the platicon microcomb as a wireless backhaul data link for multi-wavelength, high-data-rate networks utilizing high-order modulation and coherent detection.

In contrast to an independent DFB laser array, the chip-scale microcomb has a lower intrinsic optical power per comb line, constrained by the pump-to-comb line conversion efficiency, and a lower OCNR, which limits the maximum reach of the free-space link, the choice of modulation format, and the maximum symbol rate. To mitigate this limitation and the impact of ASE noise from cascaded optical amplifiers, it is essential to increase the comb line powers by optimizing the pump-to-comb-line conversion efficiencies. Figure 3c presents a parameter map comparing the conversion efficiency and 20 dB optical bandwidth across different frequency microcomb candidates. Normal dispersion microcombs, including dark-pulse microcombs and the platicon microcomb employed here, generally exhibit a trade-off between conversion efficiency and optical bandwidth.

To evaluate atmospheric effects on our free-space testbed, Fig. 3d shows the measured power fluctuations by monitoring the beam position using a quadrant position detector. This data illustrates beam position fluctuations before and after active feedback stabilization, with a 10×improvement in peak-to-peak beam position variation. To effectively suppress pointing errors in free-space, a tight beam-tracking lock system was implemented, as detailed in Methods and Supplementary Information Section IV. To further assess the BER dependence on atmospheric turbulence-induced intensity scintillation, Fig. 3e shows power fluctuations after the removal of pointing error through active beam propagation stabilization. The link availability and dropout periods before and after active stabilization are summarized in the Methods and Supplementary Information Section IV. The intensity scintillation follows a log-normal distribution, and the turbulence-induced intensity probability is characterized by the scintillation index σ_I^2, given by:

$$\sigma_I^2 = \frac{\langle I^2\rangle - \langle I\rangle^2}{\langle I\rangle^2}$$

where I is the received optical intensity. The corresponding refractive index structure parameter C_n^2 can be calculated using the Rytov variance approximation for weak turbulence: $4\sigma_I^2 \approx \sigma_R^2 = 1.23C_n^2k^{7/6}L^{11/6}$ [74], where k is the carrier wavenumber and L is the propagation distance. Based on our measurements, the $C_n^2 = 4.8\times10^{-14}m^{-2/3}$ at 1550 nm for the 160 m free-space testbed supports the communication model outlined below.

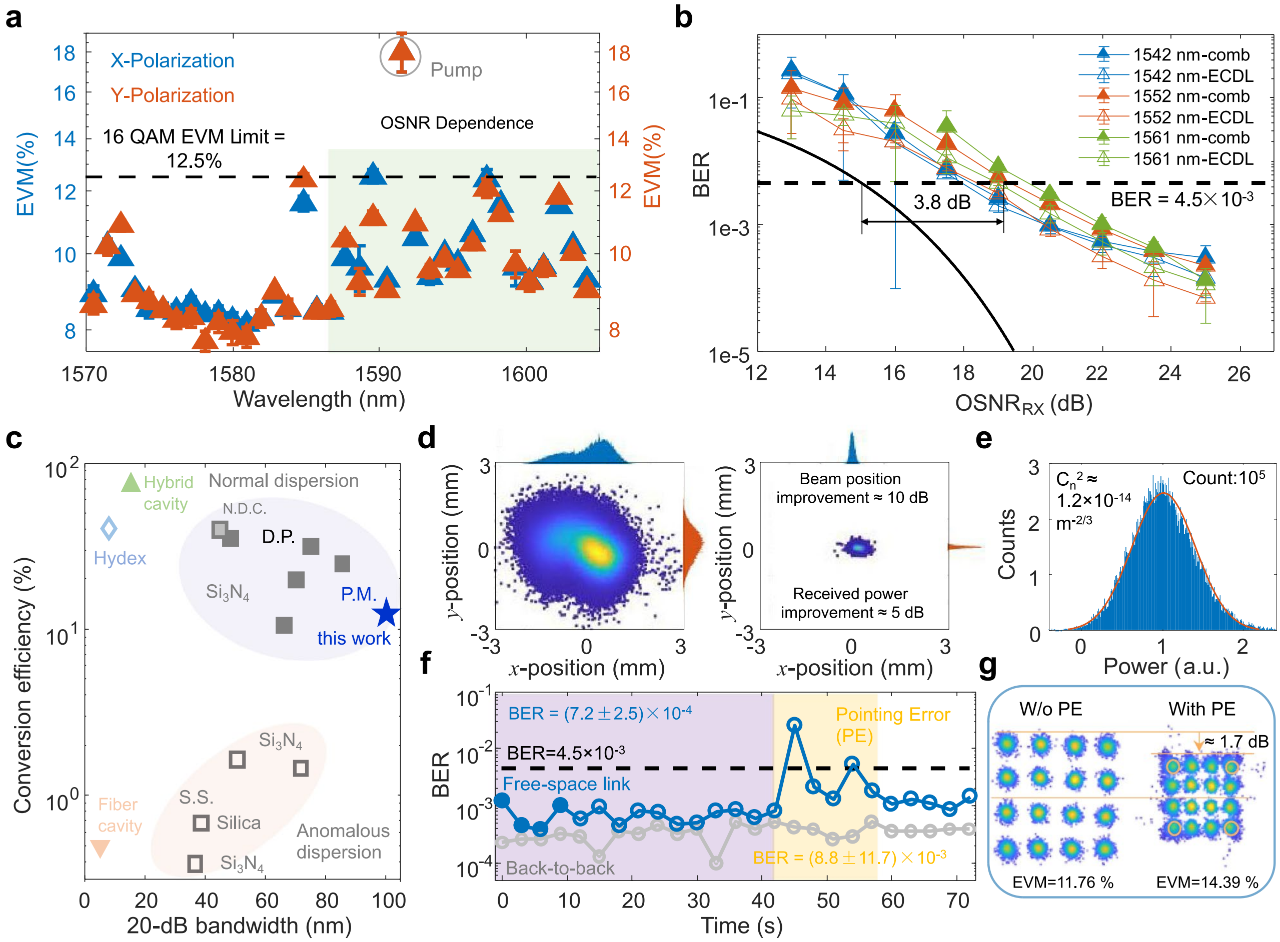

Fig. 3 WDM-PDM-based coherent data fronthaul transmission over a 160-m horizontal free-space link with testbed parameters: conversion efficiency, beam position stabilization, and atmospheric turbulence. **a** Measured EVM of each optical carrier channel across the L-band spectral range, with the error bar denoting the standard deviation. The 16QAM EVM threshold for error-free data transmission is also indicated. **b** Measured BER versus OSNR before the coherent receiver for three independent carriers (1542.93, 1552.96 and 1561.32 nm) derived from the platicon frequency microcomb (solid symbols). 16QAM signaling at 20 Gbaud for both XY polarization together is implemented. For comparison, a single-wavelength standalone ECDL (empty symbols) is also shown. A 3.8 dB power penalty is observed at the error-free data transmission threshold, compared to the theoretical BER-OSNR limit. Additionally, an ≈ 1 dB degradation in performance is observed for the multi-channel microcomb, relative to the single-wavelength ECDL. **c** Comparison of microcombs' 20-dB optical spectrum bandwidth and conversion efficiency. The conversion efficiency data is sourced from each reference, with the optical bandwidth determined by the spectrum of the comb from the maximum comb line. This comparison highlights the relationship between the 20-dB optical spectrum bandwidth and the conversion efficiency across different microcomb configurations. **S.S.**: single soliton [79, 80, 75, 75; from left-to-right]. **P.M.**: Platicon frequency microcomb [this work]. **D.P.**: dark pulse [76, 30, 59, 30, 77; from left-to-right] **N.D.C.**: normal dispersion comb [78]. Hybrid (fiber and microresonator) cavity with the laser cavity soliton [4], and Hydex with the soliton crystal with internal conversion efficiency [51]. **d** Measured free-space laser beam position along the X–Y direction using a quadrant position detector. Left panel: free-running conditions with asymmetrical beam position fluctuations. Right panel: Corresponding beam position after active feedback control. **e** Measured atmospheric turbulence-induced intensity scintillation (σ_I^2) of the free-space link field trial, after suppressing pointing errors. **f** Measured BER evolution showing the residual pointing error degradation in the free-space link, compared to a back-to-back baseline. **g** Corresponding retrieved constellation diagrams of the first four (solid symbols in panel **f**) BER sampling segment and the fluctuation BER induced by pointing error (PE) shadowed in light yellow color

Figure 3f examines the BER dependence on atmospheric turbulence and pointing errors by continuously transmitting a data sequence. Notably, the example segments (16th to 19th data points) show significant BER fluctuations due to unlocked pointing errors. Corresponding constellation diagrams, shown in Fig. 3g, reveal a ≈ 1.7 dB amplitude degradation and random symbol movement in the complex plane with unlocked PE, compared to stable conditions without PE. This power penalty characterization for the free-space coherent communication link provides key insights for point-to-point free-space data transmission. To extend the data transmission reach, improvements in

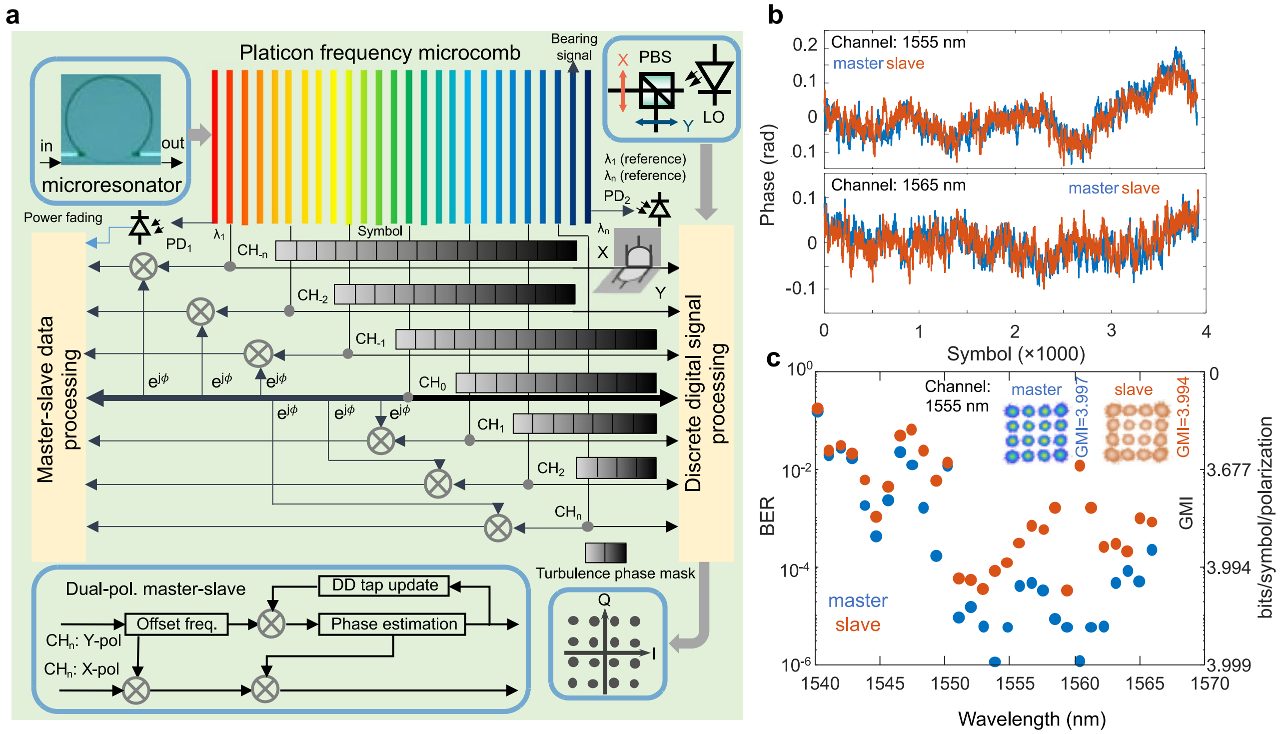

Fig. 4 Wavelength-diverse coherent architecture using chip-scale platicon microcombs in high-rate free-space optical communication links. **a** Platicon microcomb based multiple channel data transmission with discrete digital signal processing and master–slave carrier phase recovery. The bottom inset shows the dual-polarization master–slave architecture. PD: photodetector; LO: local oscillator; CH: channel; Dual-pol: dual-polarization; Offset freq: Offset frequency; X-pol: X-polarization; DD: decision directed. **b** Phase fluctuations at the X- and Y- polarizations of the 1555 nm and 1565 nm channels. **c** The obtained bit error rates with the master–slave data processing scheme. Insets: Measured constellation diagrams after the master–slave data processing, along with the calculated generalized mutual information

the OCNR of the optical carriers are necessary. This can be achieved by enhancing the frequency microcomb conversion efficiency and utilizing low-noise optical preamplifiers, which are critical for overcoming atmospheric impairments and maximizing the link's range and data rate.

3 Discussion

We further investigate the performance of the chip-scale microcomb-based optical communication link for wavelength-diverse multi-channel data transmission, focusing particularly on discrete digital signal processing and a variant of master–slave carrier recovery [52], as illustrated in Fig. 4a. The microcomb, generated within the microresonator, enables the selection of edge lines to monitor free-space channel power fading and differential channel fading. By leveraging coherent detection, polarization multiplexing, and advanced DSP techniques, our dual-polarization master–slave carrier recovery simplifies the data processing complexity in the platicon microcomb-based free-space link demonstration. In our coherent signal processing framework, we account for turbulence-induced power fading and carrier phase fluctuations, which are digitally compensated. The lower inset of Fig. 4a depicts the dual-polarization master–slave data processing scheme. Example phase fluctuations observed at the X- and Y-polarizations of the 1555 nm and 1565 nm carriers are shown in Fig. 4b, demonstrating similar phase evolutions across both polarizations. We then apply the retrieved carrier phase from the X-polarization to correct the Y-polarization. The resulting BERs using this master–slave data processing scheme are presented in Fig. 4c, with BER values dropping below 10^{-4} before error correction. Insets show example constellation maps post-signal processing. The generalized mutual information achieved with our approach ranges from around 3.677 to 3.999 bits/symbol/polarization, which is close to the ideal 4 bits/symbol asymptote for 16-QAM, based on the retrieval architecture implemented for the platicon microcomb free-space link. The proposed architecture can be applied to free-space WDM duplex wireless access networks, especially in ultra-dense small-cell deployments, where networked static and flying relay units are organized in tree-topology structures. Additionally, this architecture can be integrated with millimeter-wave links or LiDAR systems to expand the network into an Ultra-Dense WDM-FS-PON, offering scalable and high-performance communication for next-generation optical wireless networks.

4 Conclusions

We demonstrate a chip-scale microcomb-based coherent transceiver for high-capacity point-to-point and wireless fronthaul atmospheric free-space data transmission. The spectral intensity uniformity of the microcomb and its pump-to-comb-line power conversion efficiency are enhanced through optimized waveguide spatial mode interaction. First, 55 optical carriers spanning from 1540 to 1600 nm with 115 GHz carrier spacing are evaluated for PDM-WDM coherent data transmission. The system achieves an aggregated line data rate capacity of up to 8.21 Tbit/s, enabling post-correction error-free data transmission. The corresponding net spectral efficiency, normalized to the channel spacing, is 1.28 bit/s/Hz. To extend the point-to-point link into a distributed wireless multi-access network, we perform single carrier PDM coherent data transmission with 35 independent channels, exploring the potential for high-rate future networks. The PDM-FSO system provides improved noise tolerance and mitigates the impact of residual pump ASE noise. An aggregated data rate capacity up to 5.21 Tbit/s is estimated, considering a 7% FEC overhead, with the measured EVMs for the dual-polarization link remaining below the post-correction error-free threshold of 12.5%. The effects of turbulence-induced intensity scintillation and pointing error fluctuations on the free-space link are characterized by continuous monitoring of the measured BER, with degradation analyzed. For the first time, we demonstrate master–slave carrier phase retrieval for free-space coherent communication with frequency microcombs.

Data transmission performance is initially bounded by the $\mathrm{OSNR}_{\mathrm{TX}}$ and the system's ASE noise floor for short-range communication. For long-range transmission, performance is limited by channel fading, atmospheric attenuation, and intensity scintillation. The communication data rate can be further expanded by utilizing EDFAs with broader gain bandwidths and employing more advanced modulation formats within a super-channel scheme. Due to the strong correlation between stochastic frequency and phase variations of the optical carriers, joint phase estimation methods could be explored for improved system performance. To further extend the transmission range (tens of kilometers), additional improvements in both pump-to-comb-line power conversion efficiency and overall power consumption are needed by optimizing the comb generation process of the Platicon microcomb. This chip-scale transceiver platform holds significant potential for broadband connectivity, advanced Gaussian relay networks, and terrestrial or backhaul links in support of wireless networks for 5G and future 6G applications.

5 Methods and materials

CMOS-compatible silicon nitride (Si_3N_4) microresonator fabrication The microresonator is fabricated using CMOS-compatible processes. First, a 5 μm thick under-cladding SiO_2 layer is deposited onto the Si substrate. An 800 nm thick Si_3N_4 layer is then deposited by low-pressure chemical vapor deposition. This layer is patterned using optimized deep-ultraviolet lithography and etched through optimized reactive ion dry etching. To reduce waveguide propagation loss, the chip undergoes a 3-h annealing process at 1150 °C. Finally, a 3 μm thick SiO_2 layer is deposited as the upper cladding layer over the Si_3N_4 microresonator.

Platicon frequency microcomb generation The fabricated Si_3N_4 microresonator, with a free spectral range (FSR) of 115 GHz, a loaded quality factor $Q \approx 700{,}000$, and a group velocity dispersion (GVD) of 50 fs^2/mm, is used to generate the platicon frequency microcomb. The pump mode is selected at ≈ 1591 nm, where the adjacent mode (the −1st mode) experiences a significant mode shift due to higher-order mode coupling. The microresonator waveguide trapezoidal cross-section gives rise to orthogonal and transverse mode components and mode-coupling interactions. To initiate the platicon microcomb, a continuous-wave ECDL (New Focus TLB 6730), amplified by an EDFA (BKtel) up to 36 dBm, is used. The laser is filtered for TM mode pumping using a cube polarization beam splitter (PBS) and slowly tuned into resonance from the blue-detuning side. The platicon microcomb is geneated at an effective blue detuning. Experimental details, including the TM_{00} and TM_{10} cavity mode distributions, the optical spectral evolution as a function of pump-resonance detuning, the overlap of selected optical spectrum with the LLE-modeled profile, second-harmonic autocorrelation, and frequency-resolved optical gating, are shown in Fig. S2. The TM mode is selected over the TE polarization due to its normal GVD, which facilitates platicon comb formation. To suppress ASE noise from the high-power EDFA, an OBPF with a 3-dB bandwidth of ≈ 10 nm (Filter 1 in Fig. S1a) is used. Each facet of the microresonator introduces a 3-dB loss, resulting in an on-chip power of 33 dBm, which is used to generate the frequency microcomb. The output power of ≈ 30 dBm is collimated and filtered through a narrow-bandwidth fiber grating notch filter (Filter 2 in Fig. S1a) to remove the pump laser and prevent power saturation in downstream amplifiers, before being sent for data transmission measurements. Additionally, 10% of the output power is tapped off and directed to an optical spectrum analyzer (OSA, Yokogawa AQ6375B) for spectral monitoring. A microcomb power of 1 mW is sent to a photodetector (PD, Newport 1611FC-AC) with an RF bandwidth of 1 GHz to assess the intensity noise, which is measured using an electrical spectrum analyzer (ESA, Agilent MXA9020N).

Numerical simulation of Platicon microcomb formation, bandwidth scalability, and conversion efficiency calculation The platicon microcomb forms in the normal dispersion regime as a specific solution of the Lugiato-Lefever equation (LLE), which is solved after considering pump mode coupling:

$$T_R\frac{\partial}{\partial t}A(t,\tau) = \sqrt{\alpha_c}A_P - \left[\frac{\alpha_c+\alpha_p}{2} + j\delta - j\frac{\beta_2}{2}L_{cav}\frac{\partial^2}{\partial\tau^2} - j\frac{n_2\omega L_{cav}}{c}I(t,\tau)\right]A(t,\tau)$$

where T_R is the round-trip time, $A(t,\tau)$ is the electric field envelope, where t represents slow time (evolution over round trips) and τ is the fast time (temporal structure of the wave). $A_P = 0.25W$ is the external pump power, $\alpha_p = 0.0024$ is the propagation loss, $\alpha_c = 0.0048$ is the coupling loss, $L_{cav} = 1.4mm$ is the cavity length, $-0.01 \leq \delta \leq 0.1687$ is the pump-resonance detuning range, and the β_2 is set to be 50 fs^2/mm based on our experimental characterization. The mode frequency shift is incorporated through an empirical two-parameter model: $a/2/(\mu - b - 0.5)$, where a is the maximum modal frequency shift, and μ and b are the mode number and the maximum modal frequency shift, respectively. The estimated frequency shift is 0.1% of the free spectral range (FSR), which is approximately $\Delta\mu = 115$ MHz at 1591 nm, determined by comparing the simulated comb spectrum with experimental results for qualitative agreement. The simulation models 2,001 modes centered around the pump. The process starts with vacuum noise and runs for 100,000 round trips until the solution reaches a steady state. To optimize the two-shoulder optical bandwidth and conversion efficiency, mode shift magnitude and pump power are swept. Mode shift magnitude from 10 to 1,000 MHz in 5 MHz steps (at the −1st mode relative to the pump mode). Pump power from 0.1 to 1.5 W in 0.1 W steps. The conversion efficiency (defined by $\eta = P_{comb}/P_{pump} \times 100$) are optimized, where P_{comb} is the power of the comb (excluding the pump comb line), and P_{pump} is the power of the pump comb line.

Free-space data transmission The microcomb output, with a power of 7.5 dBm, is used for data transmission. It is filtered through a 4 nm fiber grating notch filter to suppress the pump laser by more than 40 dB. The filtered optical spectrum is then split into the C- and L-bands, with powers of − 5.8 dBm and 4.2 dBm, respectively. The communication experiments are conducted as follows: (1) two commercial ECDLs are first used to test the data transmission system. This ensures post-correction, error-free communication with 10^5 symbols; (2) One of the platicon microcomb lines is then coupled into the communication link for further testing; (3) To investigate the power penalty caused by the frequency microcomb compared to state-of-the-art ECDLs, a noise loading measurement is performed; (4) A back-to-back PDM-WDM communication is conducted without the free-space transmission link to validate the optical carriers over the C-band and L-band; (5) Both PDM-WDM and PDM-FSO coherent data transmissions are carried out for the C/L-band and L-band, respectively, over a 160-m atmospheric horizontal free-space link. For data generation, 16-QAM symbols are generated using raised-cosine filtering. These symbols are loaded into four high-performance AWGs (Tektronix AWG 70001B) with a sampling rate of 50 GSa/s and a vertical resolution of 10 bits. The four AWGs are synchronized with an accuracy of less than 2 ps by adjusting the phase relative to the system clock, based on the demodulated eye-diagram. The data streams are then loaded into the PDM IQ modulator (Tektronix OM5110) at the optimized bias voltages: XI = 4.74 V, XQ = 1.84 V, YI = −2.48 V, YQ = 4.35 V, XP = 11.04 V and YP = 18.78 V. The total loss, including modulator insertion and modulation losses, is ≈ 20 dB. Transmitter impairments are minimized by adjusting the relative time delay between the I and Q arms based on the skewness of the demodulated constellation diagram. The relative time delay between the X- and Y-polarizations is minimized by aligning the demodulated eye-diagram for both polarizations. The bias voltages are optimized in real-time by examining the BER and EVM. A tunable optical bandpass filter (OBPF, EXFO XTA-50) is used to center each optical carrier within a 3 nm bandwidth for data demodulation. The received optical signal is first polarization-demultiplexed, then coherently detected using a tunable ECDL (Santec TLS-510) at an output power of 11 dBm. Two synchronized high-performance real-time oscilloscopes (Tektronix DPO70000SX) are used to digitize the waveforms of the four signals (XI, XQ, YI, YQ) at a sampling rate of 100 GSa/s. This process is repeated for 55 comb lines of the platicon frequency microcomb (with a total of 64 lines available for the multiple access fronthaul network implementation).

Digital signal processing DSP is employed to analyze key metrics of the data transmission system, including the demodulated BER, constellation diagram, quality factor (Q), and eye diagram. These metrics help optimize the system for post-correction, enabling error-free communication (detailed setup provided in Supplementary II). To decode the data sequence from the digitized waveforms, it is required to minimize transmitter impairments, coherent receiver non-idealities, and free-space link pointing errors. Through iterative optimization, the system parameters are refined to achieve post-correction for error-free data transmission. The data packet size is limited to 5 µs (100,000 symbols), constrained by the memory depth of the AWGs. A raised cosine filter with a roll-off factor of 0.5 is applied for pulse shaping of the synthesized 16-QAM signal, helping to suppress intersymbol interference (ISI). The AWGs operate at a sampling rate of 50 GSa/s, transmitting a bit sequence of length 2^{15}. Receiver impairments are mitigated in two stages: first, by calibrating the RF frequency responses of the coherent receiver, and second, by compensating for the relative time delay between the four channels of the coherent receiver. The IQ time imbalance is corrected using Gram-Schmidt orthogonalization. To further improve signal quality, oscilloscopes resample the received waveform at five times the symbol rate. Polarization demultiplexing is performed using a Jones matrix-based polarization calibration estimator. Clock frequency recovery is set to 20 GHz. Additionally, an intradyne frequency offset estimator and a blind-phase search method are used to evaluate the frequency difference and phase jitter between the microcomb optical carrier and the local optical oscillator. A fourth-order raised cosine filter, with a roll-off factor of 0.05 and a cutoff frequency of 15 GHz, is applied for matched filtering, effectively suppressing electrical noise and ASE noise. The performance metrics—BER, EVM, and Q-factor—are utilized to assess the quality of the data transmission.

Noise loading Individual microcomb lines, each with a power of −10 dBm, are selected for power penalty measurements (detailed setup provided in Supplementary II). An ASE source with an output power of 7 dBm is used to introduce noise, which is then amplified by an EDFA to ≈ 13 dBm. The noise loading measurement is conducted by gradually adjusting the power ratio between the noise and the optical carrier, while keeping the total average power constant. For comparison, a standalone ECDL replaces the microcomb line, maintaining the same wavelength and power.

Turbulence characterization and pointing error suppression The beam size (≈ 4 mm) of the collimated optical signal (Thorlabs F280APC-1550) is expanded using an achromatic Galilean beam expander (Thorlabs GBE10-C) with a 10× expansion ratio (detailed setup in Supplementary Information Section III). The beam-expanded optical signal is then injected into a 160-m free-space link. A beam reducer is employed to reduce the received signal's beam size back to ≈ 4 mm by optimizing the focal lengths of the beam expander and reducer. The reduced optical signal is subsequently split into two parts with a power ratio of 10:90 using a beam splitter (Thorlabs BS030). One portion is directed into the coherent receiver, while the other is fed into a quadrant detector sensor (Thorlabs PDQ30C) via an achromatic doublet focusing lens (Thorlabs AC254-050-C) for active beam stabilization. By optimizing the PID controller parameters, the beam stabilization system operates continuously for over 10 h without requiring relocking, with a locking bandwidth of ≈ 10 kHz.

Abbreviations

FSO communication	Free-space optical communication
DSP	Digital signal processing
OCNR	Optical carrier-to-noise ratio
EVM	Error vector magnitude
PE	Pointing error
FEC	Forward error correction

Supplementary Information

The online version contains supplementary material available at https://doi.org/10.1186/s43593-025-00082-0.

Supplementary file 1.

Acknowledgements

The authors acknowledge discussions with Rob Marsland along with system debugging and instruments support, and initial measurements with Xinghe Jiang.

Author contributions

W.W., J.W., and H.L. designed and led the project. W.W., H.L., J.W., J.F.M., H.Y., and D.S.K. conducted the measurements. F.H., Y.H.E, C.F., D.-I.L., W.Z.L. and W.W examined the channel modeling. J.Y. designed the microresonator, and M.Y. and D.-L.K. performed the device nanofabrication. W.W. and H.L. analyzed the data. W.W., D.-I.L., H.L., A.K.V and C.W.W. wrote the manuscript, with contributions from all authors.

Funding

We acknowledge financial support from the Office of Naval Research (N00014-16-1-2094), and the National Science Foundation (1824568, 1810506, 1741707, and 1919355).

Data availability

The data that support the results of this study are available from the corresponding author upon reasonable request.

Declarations

Competing interests

The authors declare that they have no conflict of interest.

Received: 1 November 2024 Revised: 17 February 2025 Accepted: 20 February 2025

References

1. Y. Liu, Z. R. Qiu, X. R. Ji, A. Bancora, G. Lihachev, J. Riemensberger, R. N. Wang, A. Voloshin, and T. J. Kippenberg. A fully hybrid integrated erbium-based laser. Nat. Photon. 18, 829–835 (2024)
2. Y. Liu, Z. R. Qiu, X. R. Ji, A. Lukashchuk, J. J. He, J. Riemensberger, M. Hafermann, R. N. Wang, J. Q. Liu, C. Ronning, T. J. Kippenberg. A photonic integrated circuit–based erbium-doped amplifier. Science 376, 1309–1313 (2022)
3. P. Del'Haye, A. Schliesser, O. Arcizet, T. Wilken, R. Holzwarth, T.J. Kippenberg. Optical frequency comb generation from a monolithic microresonator. Nature 450, 1214–1217 (2007)
4. C. Xiang, J. Q. Liu, J. Guo, L. Chang, R. N. Wang, W. L. Weng, J. Peters. W. Q. Xie, Z. Y. Zhang, J. Riemensberger, J. Selvidge, T. J. Kippenberg, and J. E. Bowers. Laser soliton microcombs heterogeneously integrated on silicon. Science 373, 99–103 (2021)
5. S.A. Diddams, K. Vahala, T. Udem. Optical frequency combs: coherently uniting the electromagnetic spectrum. Science 369, 267 (2020)
6. Y. Shi, X. Li, G. Y. Chen, M. J. Zou, H. J. Cai, Y. Yu, and X. L. Zhang. Avalanche photodiode with ultrahigh gain bandwidth product of 1033 GHz. Nat. Photon. 18, 610–616 (2024)
7. C. L. Wang, Z. H. Li, J. Riemensberger, G. Lihachev, M. Churaev, W. Kao, X. R. Ji, J. Y. Zhang, T. Blesin, A. Davydova, Y. Chen, K. Huang, X. Wang, X. Ou, and T. J. Kippenberg. Lithium tantalate photonic integrated circuits for volume manufacturing. Nature 629, 784–790 (2024)
8. C. Wang, M. Zhang, X. Chen, M. Bertrand, A. Shams-Ansari, S. Chandrasekhar, P. Winzer, and M. Lončar. Integrated lithium niobate electro-optic modulators operating at CMOS-compatible voltages. Nature 562, 101–104 (2018)
9. A. Rizzo, A. Novick, V. Gopal, B.Y. Kim, X.C. Ji, S. Daudlin, Y. Okawachi, Q.X. Cheng, M. Lipson, A.L. Gaeta, K. Bergman, Massively scalable Kerr comb-driven silicon photonic link. Nat. Photon. 17, 781–790 (2023)
10. C.B. Zhang, Y.X. Zhu, B.B. He, J.J. Lin, R.W. Liu, Y.C. Xu, L.L. Yi, Q.B. Zhuge, W.W. Hu, W.S. Hu, Z.Y. Chen, X.P. Xie, Clone-comb-enabled high-capacity digital-analogue fronthaul with high-order modulation formats. Nat. Photon. 17, 1000–1008 (2023)
11. M.Z. Chowdhury, M. Shahjalal, S. Ahmed, Y.M. Jang, 6G wireless communication systems: Applications, requirements, technologies, challenges, and research directions. IEEE Open J. Commun. Soc. 1, 957–975 (2020)
12. I.F. Akyildiz, A. Kak, S. Nie, 6G and beyond: the future of wireless communications systems. IEEE access 8, 133995–134030 (2020)
13. K. Liu, Y. Feng, C. Han, B. Chang, Z. Chen, Z. Xu, L. Li, B. Zhang, Y. Wang, Q. Xu, High-speed 0.22 THz communication system with 84 Gbps for real-time uncompressed 8K video transmission of live events. Nat. Commun. 15, 8037 (2024)
14. T. Nagatsuma, G. Ducournau, C.C. Renaud, Advances in terahertz communications accelerated by photonics. Nat. Photon. 10, 371–379 (2016)
15. S. Koenig, D. Lopez-Diaz, J. Antes, F. Boes, R. Henneberger, A. Leuther, A. Tessmann, R. Schmogrow, D. Hillerkuss, R. Palmer, T. Zwick, C. Koos, W. Freude, O. Ambacher, J. Leuthold, I. Kallfass, Wireless sub-THz communication system with high data rate. Nat. Photon. **7**, 977–981 (2013)
16. Y. Salamin, B. Baeuerle, W. Heni, F.C. Abrecht, A. Josten, Y. Fedoryshyn, C. Haffner, R. Bonjour, T. Watanabe, M. Burla, D.L. Elder, L.R. Dalton, J. Leuthold, Microwave plasmonic mixer in a transparent fibre–wireless link. Nat. Photon. 12, 749–753 (2018)
17. H. Kaushal, G. Kaddoum, Optical communication in space: challenges and mitigation techniques. IEEE Commun. Surv. Tutor. 19, 57–96 (2016)
18. Y.-A. Chen, Q. Zhang, T.-Y. Chen, W.-Q. Cai, S.-K. Liao, J. Zhang, K. Chen, J. Yin, J.-G. Ren, Z. Chen, S.-L. Han, Q. Yu, K. Liang, F. Zhou, X. Yuan, M.-S. Zhao, T.-Y. Wang, X. Jiang, L. Zhang, W.-Y. Liu, Y. Li, Q. Shen, Y. Cao, C.-Y. Lu, R. Shu, J.-Y. Wang, L. Li, N.-L. Liu, F.H. Xu, X.-B. Wang, C.-Z. Peng, J.-W. Pan, An integrated space-to-ground quantum communication network over 4600 kilometres. Nature (2021)
19. H.J. Kang, J.W. Yang, B.J. Chun, H. Jang, B.S. Kim, Y.J. Kim, S.W. Kim, Free-space transfer of comb-rooted optical frequencies over an 18 km open-air link. Nat. Commun. 10, 4438 (2019)
20. J.W. Yang, D.I. Lee, D.C. Shin, J.H. Lee, B.S. Kim, H.J. Kang, Y.J. Kim, S.W. Kim, Frequency comb-to-comb stabilization over a 1.3-km free-space atmospheric optical link. Light Sci. Appl. **11**, 253 (2022)
21. M.P.J. Lavery, M.M. Abadi, R. Bauer, G. Brambilla, L. Cheng, M.A. Cox, A. Dudley, A.D. Ellis, N.K. Fontaine, A.E. Kelly, C. Marquardt, S. Matlhane, B. Ndagano, F. Petruccione, R. Slavík, F. Romanato, C. Rosales-Guzmán, F.S. Roux, K. Roux, J. Wang, A. Forbes, Tackling Africa's digital divide. Nat. Photon. 12, 249–252 (2018)
22. A. Dochhan, J. Poliak, J. Surof, M. Richerzhagen, H. F. Kelemu, and R. M. Calvo, 13.16 Tbit/s free-space optical transmission over 10.45 km for geostationary satellite feeder-links. *Photonic Networks*, 20th ITG-Symposium (2019).
23. E. Ciaramella, Y. Arimoto, G. Contestabile, M. Presi, A. D'Errico, V. Guarino, M. Matsumoto, 1.28 Terabit/s (32×40 Gbit/s) WDM transmission system for free space optical communications. IEEE J. Sel. Areas Commun. 27, 1639–1645 (2009)
24. J. Wang, J.-Y. Yang, I.M. Fazal, N. Ahmed, Y. Yan, H. Huang, Y.X. Ren, Y. Yue, S. Dolinar, M. Tur, A.E. Willner, Terabit free-space data transmission employing orbital angular momentum multiplexing. Nat. Photon. 6, 488–496 (2012)
25. T. Harter, C. Füllner, J.N. Kemal, S. Ummethala, J.L. Steinmann, M. Brosi, J.L. Hesler, E. Bründermann, A.-S. Müller, W. Freude, S. Randel, C. Koos, Generalized Kramers-Kronig receiver for coherent terahertz communications. Nat. Photon. 14, 601–606 (2020)
26. N.B. Zhao, X.Y. Li, G.F. Li, J.M. Kahn, Capacity limits of spatially multiplexed free-space communication. Nat. Photon. 9, 822–826 (2015)
27. A. Pasquazi, M. Peccianti, L. Razzari, D. J. Moss, S. Coen, M. Erkintalo, Y. K. Chembo, T. Hansson, S. Wabnitz, P. Del'Haye, X. Xue, A. M. Weiner, and R. Morandotti, Micro-combs: A novel generation of optical sources. *Phys. Rep*, 729, 1–81 (2018).
28. B. C. Yao W. T. Wang, Z. D. Xie, Q. Zhou, T. Tan, H. Zhou, G. C. Guo, S. N. Zhu, N. H. Zhu, and C. W. Wong, Interdisciplinary advances in microcombs: bridging physics and information technology. *eLight* 4, 19 (2024).
29. T. Herr, V. Brasch, J.D. Jost, C.Y. Wang, N.M. Kondratiev, M.L. Gorodetsky, T.J. Kippenberg, Temporal solitons in optical microresonators. Nat. Photon. 8, 145–152 (2013)
30. X.X. Xue, P.-H. Wang, Y. Xuan, M.H. Qi, A.M. Weiner, Microresonator Kerr frequency combs with high conversion efficiency. Laser Photon. Rev. 11, 1600276 (2017)
31. G. Lihachev, W.L. Weng, J.Q. Liu, L. Chang, J. Guo, J.J. He, R.N. Wang, M.H. Anderson, Y. Liu, J.E. Bowers, T.J. Kippenberg, Platicon microcomb generation using laser self-injection locking. Nat. Commun. 13, 1771 (2022)
32. W.T. Wang, A. Aldhafeeri, H. Zhou, T. Melton, X.H. Jiang, A.K. Vinod, M. Yu, G.-Q. Lo, D.-L. Kwong, C.W. Wong, Polarization-diverse soliton transitions and deterministic switching dynamics in strongly-coupled and self-stabilized microresonator frequency combs. Commun. Phys. 7, 279 (2024)
33. G. Moille, M. Leonhardt, D. Paligora, N. Englebert, F. Leo, J. Fatome, K. Srinivasan, M. Erkintalo, Parametrically driven pure-Kerr temporal solitons in a chip-integrated microcavity. Nat. Photon. 18, 617–624 (2024)
34. E. Lucas, S.-P. Yu, T.C. Briles, D.R. Carlson, S.B. Papp, Tailoring microcombs with inverse-designed, meta-dispersion microresonators. Nat. Photon. 17, 943–950 (2023)
35. S.-W. Huang, H. Zhou, J.H. Yang, J.F. McMillan, A. Matsko, M. Yu, D.-L. Kwong, L. Maleki, C.W. Wong, Mode-locked ultrashort pulse generation from on-chip normal dispersion microresonators. Phys. Rev. Lett. 114, 053901 (2015)
36. D.T. Spencer, T. Drake, T.C. Briles, J. Stone, L.C. Sinclair, C. Fredrick, Q. Li, D. Westly, B.R. Ilic, A. Bluestone, N. Volet, T. Komljenovic, L. Chang, S.H. Lee, D.Y. Oh, M.G. Suh, K.Y. Yang, M.P. Pfeiffer, T.J. Kippenberg, E. Norberg, L. Theogarajan, K. Vahala, N.R. Newbury, K. Srinivasan, J.E. Bowers, S.A. Diddams, S.B. Papp, An optical-frequency synthesizer using integrated photonics. Nature 557, 81–85 (2018)
37. S.-W. Huang, J.H. Yang, M. Yu, B.H. McGuyer, D.-L. Kwong, T. Zelevinsky, C.W. Wong, A broadband chip-scale optical frequency synthesizer at 2.7×10^{-16} relative inaccuracy. Sci. Adv. 2, e1501489 (2016)
38. E. Obrzud, M. Rainer, A. Harutyunyan, M.H. Anderson, M. Geiselmann, B. Chazelas, S. Kundermann, S. Lecomte, M. Cecconi, A. Ghedina, E. Molinari, F. Pepe, F. Wildi, F. Bouchy, T.J. Kippenberg, T. Herr, A microphotonic astrocomb. Nat. Photon. 13, 31–35 (2019)
39. M.G. Suh, X. Yi, Y.-H. Lai, S. Leifer, I.S. Grudinin, G. Vasisht, E.C. Martin, M.P. Fitzgerald, G. Doppmann, J. Wang, D. Mawet, S.B. Papp, S.A. Diddams, C. Beichman, K.J. Vahala, Searching for exoplanets using a microresonator astrocomb. Nat. Photon. 13, 25–30 (2019)
40. M.G. Suh, Q.-F. Yang, K.Y. Yang, X. Yi, K.J. Vahala, Microresonator soliton dual-comb spectroscopy. Science 354, 600–603 (2016)

41. A. Dutt, C. Joshi, X.C. Ji, J. Cardenas, Y. Okawachi, K. Luke, A.L. Gaeta, M. Lipson, On-chip dual-comb source for spectroscopy. Sci. Adv. 2, e1701858 (2018)
42. M.J. Yu, Y. Okawachi, A.G. Griffith, N. Picqué, M. Lipson, A.L. Gaeta, Silicon-chip-based mid-infrared dual-comb spectroscopy. Nat. Commun. 9, 1869 (2018)
43. Y.-S. Jang, H. Liu, J.H. Yang, M.B. Yu, D.L. Kwong, C.W. Wong, Nanometric precision distance metrology via hybrid spectrally-resolved and homodyne interferometry in a single soliton frequency microcomb. Phys. Rev. Lett. 126, 023903 (2021)
44. M.G. Suh, K.J. Vahala, Soliton microcomb range measurement. Science 359, 884–887 (2018)
45. P. Trocha, M. Karpov, D. Ganin, M.H.P. Pfeiffer, A. Kordts, S. Wolf, J. Krockenberger, P.M. Palomo, C. Weimann, S. Randel, W. Freude, T.J. Kippenberg, C. Koos, Ultrafast optical ranging using microresonator soliton frequency combs. Science 359, 887–891 (2018)
46. J. Riemensberger, A. Lukashchuk, M. Karpov, W.L. Weng, E. Lucas, J.Q. Liu, T.J. Kippenberg, Massively parallel coherent laser ranging using a soliton microcomb. Nature 581, 164–170 (2020)
47. T. Tetsumoto, T. Nagatsuma, M.E. Fermann, G. Navickaite, M. Geiselmann, A. Rolland, Optically referenced 300 GHz millimetre-wave oscillator. Nat. Photon. 15, 516–522 (2021)
48. B. Wang, J.S. Morgan, K. Sun, M. Jahanbozorgi, Z. Yang, M. Woodson, S. Estrella, A. Beling, X. Yi, Towards high-power, high-coherence, integrated photonic mmWave platform with microcavity solitons. Light Sci. Appl. 10(4), 1 (2021)
49. W. Wang, P.K. Lu, A.K. Vinod, D. Turan, J.F. McMillan, H. Liu, M. Yu, D.L. Kwong, M. Jarrahi, C.W. Wong, Coherent terahertz radiation with 2.8-octave tunability through chip-scale photomixed microresonator optical parametric oscillation. Nat. Commun. 13, 5123 (2022)
50. A. Aldhafeeri, H.-H. Chin, T. Melton, D.I. Lee, A. Chu, W.T. Wang, M.B. Yu, P.G.-Q. Lo, D.-L. Kwong, C.W. Wong, Low phase noise K-band signal generation using polarization diverse single-soliton integrated microcombs. Photon. Res. 12, 1175–1185 (2024)
51. I. Kudelin, W. Groman, Q.-X. Ji, J. Guo, M.L. Kelleher, D. Lee, T. Nakamura, C.A. McLemore, P. Shirmohammadi, S. Hanifi, H.T. Cheng, N.J. Jin, L. Wu, S. Halladay, Y.Z. Luo, Z.W. Dai, W. Jin, J.W. Bai, Y.F. Liu, W. Zhang, C. Xiang, L. Chang, V. Iltchenko, O. Miller, A. Matsko, S.M. Bowers, P.T. Rakich, J.C. Campbell, J.E. Bowers, K.J. Vahala, F. Quinlan, S.A. Diddams, Photonic chip-based low-noise microwave oscillator. Nature 627, 534–539 (2024)
52. S.M. Sun, B.C. Wang, K.K. Liu, M.W. Harrington, F. Tabatabaei, R.X. Liu, J.W. Wang, S. Hanifi, J.S. Morgan, M. Jahanbozorgi, Z.J. Yang, S.M. Bowers, P.A. Morton, K.D. Nelson, A. Beling, D.J. Blumenthal, X. Yi, Integrated optical frequency division for microwave and mmWave generation. Nature 627, 540–545 (2024)
53. Y. Zhao, J.K. Jang, G.J. Beals, K.J. McNulty, X.C. Ji, Y. Okawachi, M. Lipson, A.L. Gaeta, All-optical frequency division on-chip using a single laser. Nature 627, 546–552 (2024)
54. J. Feldmann, N. Youngblood, M. Karpov, H. Gehring, X. Li, M. Stappers, M. Le Gallo, X. Fu, A. Lukashchuk, A.S. Raja, J. Liu, C.D. Wright, A. Sebastian, T.J. Kippenberg, W.H.P. Pernice, H. Bhaskaran, Parallel convolutional processing using an integrated photonic tensor core. Nature 589, 52–58 (2021)
55. X.Y. Xu, M.X. Tan, B. Corcoran, J.Y. Wu, A. Boes, T.G. Nguyen, S.T. Chu, B.E. Little, D.G. Hicks, R. Morandotti, A. Mitchell, D.J. Moss, 11 TOPS photonic convolutional accelerator for optical neural networks. Nature 589, 44–51 (2021)
56. P. Marin-Palomo, J.N. Kemal, M. Karpov, A. Kordts, J. Pfeifle, M.H.P. Pfeiffer, P. Trocha, S. Wolf, V. Brasch, M.H. Anderson, R. Rosenberger, K. Vijayan, W. Freude, T.J. Kippenberg, C. Koos, Microresonator-based solitons for massively parallel coherent optical communications. Nature 546, 274–279 (2017)
57. S. Fujii, S. Tanaka, T. Ohtsuka, S. Kogure, K. Wada, H. Kumazaki, S. Tasaka, Y. Hashimoto, Y. Kobayashi, T. Araki, K. Furusawa, N. Sekine, S. Kawanishi, T. Tanabe, Dissipative Kerr soliton microcombs for FEC-free optical communications over 100 channels. Opt. Express 30, 1351–1364 (2022)
58. A. Fülöp, M. Mazur, A. Lorences-Riesgo, Ó.B. Helgason, P.-H. Wang, Y. Xuan, D.E. Leaird, M.H. Qi, P.A. Andrekson, A.M. Weiner, V. Torres-Company, High-order coherent communications using mode-locked dark-pulse Kerr combs from microresonators. Nat. Commun. 9, 1598 (2018)
59. B. Corcoran, M.X. Tan, X.Y. Xu, A. Boes, J.Y. Wu, T.G. Nguyen, S.T. Chu, B.E. Little, R. Morandotti, A. Mitchell, D.J. Moss, Ultra-dense optical data transmission over standard fibre with a single chip source. Nat. Commun. 11, 2568 (2020)
60. L. Lundberg, M. Mazur, A. Mirani, B. Foo, J. Schröder, V. Torres-Company, M. Karlsson, P.A. Andrekson, Phase-coherent lightwave communications with frequency combs. Nat. Commun. 11, 201 (2020)
61. X.G. Zhang, Z.X. Zhou, Y.J. Guo, M.X. Zhuang, W. Jin, B.T. Shen, Y.J. Chen, J.H. Huang, Z.H. Tao, M. Jin, R.X. Chen, Z.F. Ge, Z. Fang, N. Zhang, Y.D. Liu, P.F. Cai, W.W. Hu, H.W. Shu, D. Pan, J.E. Bowers, X.J. Wang, L. Chang, High-coherence parallelization in integrated photonics. Nat. Commun. 15, 7892 (2024)
62. Y. Geng, H. Zhou, X. Han, W. Cui, Q. Zhang, B. Liu, G. Deng, Q. Zhou, K. Qiu, Coherent optical communications using coherence cloned Kerr soliton microcombs. Nat. Commun. 13, 1070 (2022)
63. A.A. Jørgensen, D. Kong, M.R. Henriksen, F. Klejs, Z. Ye, Ò.B. Helgason, H.E. Hansen, H. Hu, M. Yankov, S. Forchhammer, P. Andrekson, A. Larsson, M. Karlsson, J. Schröder, Y. Sasaki, K. Aikawa, J.W. Thomsen, T. Morioka, M. Galili, V. Torres-Company, L.K. Oxenløwe, Petabit-per-second data transmission using a chip-scale microcomb ring resonator source. Nat. Photon. 16, 798–802 (2022)
64. B. J. Puttnam, R. S. Luís, W. Klaus, J. Sakaguchi, J. M. D. Mendinueta, Y. Awaji, N. Wada, Y. Tamura, T. Hayashi, M. Hirano, and J. Marciante, 2.15 Pb/s transmission using a 22 cores homogeneous single-mode multi-core fiber and wideband optical comb. In 2015 *European Conference on Optical Communication (ECOC)* paper PDP.3.1 (2015).
65. K.Y. Yang, C. Shirpurkar, A.D. White, J.Z. Zang, L. Chang, F. Ashtiani, M.A. Guidry, D.M. Lukin, S.V. Pericherla, J. Yang, H. Kwon, J. Lu, G.H. Ahn, K.V. Gasse, Y. Jin, S.-P. Yu, T.C. Briles, J.R. Stone, D.R. Carlson, H. Song, K.H. Zou, H.B. Zhou, K. Pang, H. Hao, L. Trask, M.X. Li, A. Netherton, L. Rechtman, J.S. Stone, J.L. Skarda, L. Su, D. Vercruysse, J.-P.W. MacLean, S. Aghaeimeibodi, M.-J. Li, D.A.B. Miller, D.M. Marom, A.E. Willner, J.E. Bowers, S.B. Papp, P.J. Delfyett, F. Aflatouni, J. Vučković, Multi-dimensional data transmission using inverse designed silicon photonics and microcombs. Nat. Commun. 13, 7862 (2022)
66. H.W. Shu, L. Chang, Y.S. Tao, B.T. Shen, W.Q. Xie, M. Jin, A. Netherton, Z.H. Tao, X.G. Zhang, R.X. Chen, B.W. Bai, J. Qin, S.H. Yu, X.J. Wang, J.E. Bowers, Microcomb-driven silicon photonic systems. Nature 605, 457–463 (2022)
67. Y.B. Liu, H.Y. Zhang, J.C. Liu, L.J. Lu, J.B. Du, Y. Li, Z.Y. He, J.P. Chen, L.J. Zhou, A.W. Poon, Parallel wavelength-division-multiplexed signal transmission and dispersion compensation enabled by soliton microcombs and microrings. Nat. Commun. 15, 3645 (2024)
68. D.M. Kong, Y. Liu, Z.Q. Ren, Y.M. Jung, C. Kim, Y. Chen, N.V. Wheeler, M.N. Petrovich, M.H. Pu, K. Yvind, M. Galili, L.K. Oxenløwe, D.J. Richardson, H. Hu, Super-broadband on-chip continuous spectral translation unlocking coherent optical communications beyond conventional telecom bands. Nat. Commun. 13, 4139 (2022)
69. S.W. Jia, Z. Xie, W. Shao, Y. Wang, Y.C. He, D.Q. Zhang, P.X. Liao, W.Q. Wang, D.R. Gao, W. Wang, X.P. Xie, 150 Gbit/s 1 km high-sensitivity FSO communication outfield demonstration based on a soliton microcomb. Opt. Express 30, 35300 (2022)
70. W. Shao, Y. Wang, S.W. Jia, Z. Xie, D.R. Gao, W. Wang, D.Q. Zhang, P.X. Liao, B.E. Little, S.T. Chu, W. Zhao, W.F. Zhang, W.Q. Wang, X.P. Xie, Terabit FSO communication based on a soliton microcomb. Photon. Res. 10, 2802 (2022)
71. V.E. Lobanov, G. Lihachev, T.J. Kippenberg, M.L. Gorodetsky, Frequency combs and platicons in optical microresonators with normal GVD. Opt. Express 23, 7713 (2015)
72. R. Schmogrow, B. Nebendahl, M. Winter, A. Josten, D. Hillerkuss, S. Koenig, J. Meyer, M. Dreschmann, M. Huebner, C. Koos, J. Becker, W. Freude, J. Leuthold, Error vector magnitude as a performance measure for advanced modulation formats. IEEE Photon. Technol. Lett. 24, 61–63 (2012)
73. J. Pfeifle, V. Brasch, M. Lauermann, Y. Yu, D. Wegner, T. Herr, K. Hartinger, P. Schindler, J. Li, D. Hillerkuss, R. Schmogrow, Coherent terabit communications with microresonator Kerr frequency combs. Nat. Photon 8, 375–380 (2014)
74. A.A. Farid, S. Hranilovic, Outage capacity optimization for free-space optical links with pointing errors. J. Light. Technol. 25, 1702–1710 (2007)

75. J. Liu, A.S. Raja, M. Karpov, B. Ghadiani, M.H.P. Pfeiffer, B. Du, N.J. Engelsen, H.R. Guo, M. Zervas, T.J. Kippenberg, Ultralow-power chip-based soliton microcombs for photonic integration. Optica 5, 1347–1353 (2018)
76. Ó. B. Helgason, F. R. Arteaga-Sierra, Z. C. Ye, K. Twayana, P. A. Andrekson, M. Karlsson, J. Schröder, V. Torres-Company, Dissipative solitons in photonic molecules. Nat. Photon. 15, 305–310 (2021)
77. E. Nazemosadat, A. Fülöp, Ó.B. Helgason, P.-H. Wang, Y. Xuan, D.E. Leaird, M.H. Qi, E. Silvestre, A.M. Weiner, V. Torres-Company, Switching dynamics of dark-pulse Kerr comb states in optical microresonators. Phys. Rev. A 103, 013513 (2021)
78. B.Y. Kim, Y. Okawachi, J.K. Jang, M.J. Yu, X.C. Ji, Y. Zhao, C. Joshi, M. Lipson, A.L. Gaeta, Turn-key, high-efficiency Kerr comb source. Opt. Lett. 44, 4475–4478 (2019)
79. J.Q. Liu, E. Lucas, A.S. Raja, J.J. He, J. Riemensberger, R.N. Wang, M. Karpov, H.R. Guo, R. Bouchand, T.J. Kippenberg, Photonic microwave generation in the X- and K-band using integrated soliton microcombs. Nat. Photon 14, 486–491 (2020)
80. X. Yi, Q.-F. Yang, K.Y. Yang, M.-G. Suh, K. Vahala, Soliton frequency comb at microwave rates in a high-Q silica microresonator. Optica 2, 1078–1085 (2015)

Supplementary Information

Free-space terabits/s coherent optical links via platicon frequency microcombs

Wenting Wang[1,2,*,†], Hao Liu[1,†], Jiagui Wu[1,†], James F. McMillan[1,†], Dong-Il Lee[1,*], Futai Hu[1], Wenzheng Liu[1], Jinghui Yang[1], Hangbo Yang[1], Abhinav Kumar Vinod[1], Yahya H. Ezzeldin[3], Christina Fragouli[3], Mingbin Yu[4,5], Patrick Guo-Qiang Lo[4,6], Dim-Lee Kwong[4], Devin S. Kahrs[7], Ninghua Zhu[8], and Chee Wei Wong[1,*]

[1] Fang Lu Mesoscopic Optics and Quantum Electronics Laboratory, University of California, Los Angeles, CA 90095, United States of America

[2] Mesoscopic Optics and Advanced Instruments Laboratory, School of Optics and Photonics, Beijing Institute of Technology, Beijing, China

[3] Algorithmic Research in Network Information, University of California, Los Angeles, CA 90095, United States of America

[4] Institute of Microelectronics, A*STAR, Singapore 117865, Singapore

[5] State Key Laboratory of Functional Materials for Informatics, Shanghai Institute of Microsystem and Information Technology, Shanghai, China

[6] Advanced Micro Foundry, Singapore 117685, Singapore

[7] Tektronix, Santa Clara, CA 95054, United States of America

[8] Institute of Intelligent Photonics, Nan Kai University, Tianjin, China

[†] these authors contributed equally to this work

[*] email correspondence:wentingwang@ucla.edu; dilee@ucla.edu; cheewei.wong@ucla.edu

Supplementary Information Content

I. Platicon frequency microcomb generation and characterization

Figure S1 shows the experimental setup of the 115 GHz platicon frequency microcomb generation and characterization for the free space data transmission experiment. The normal dispersion microcomb is generated by pumping a silicon nitride microresonator with an external cavity diode laser (ECDL). A polarization controller (PC) and a polarized beam splitter (PBS) are placed before the microresonator to optimize the pump polarization at the TM polarization. The pump light is amplified by an Er-doped fiber amplifier (EDFA) at an output power up to 36.5 dBm. After the EDFA, a free-space bandpass filter (BPF) is applied to suppress amplified stimulated emission (ASE) noise. A pair of achromatic lenses is applied to couple light into and out of the microresonator, with approximate 3-dB loss per facet. Then the coupled-out light is collected into a series of fiber links through a free space collimator. The collected light is divided into several paths for further characterization and application, while the majority (99%) is sent for data transmission, and the remaining light is used for monitoring the optical spectrum, intensity noise (DC to 1 GHz) and output power, with an optical spectrum analyzer (OSA), electric spectrum analyzer (ESA) and power meter, respectively.

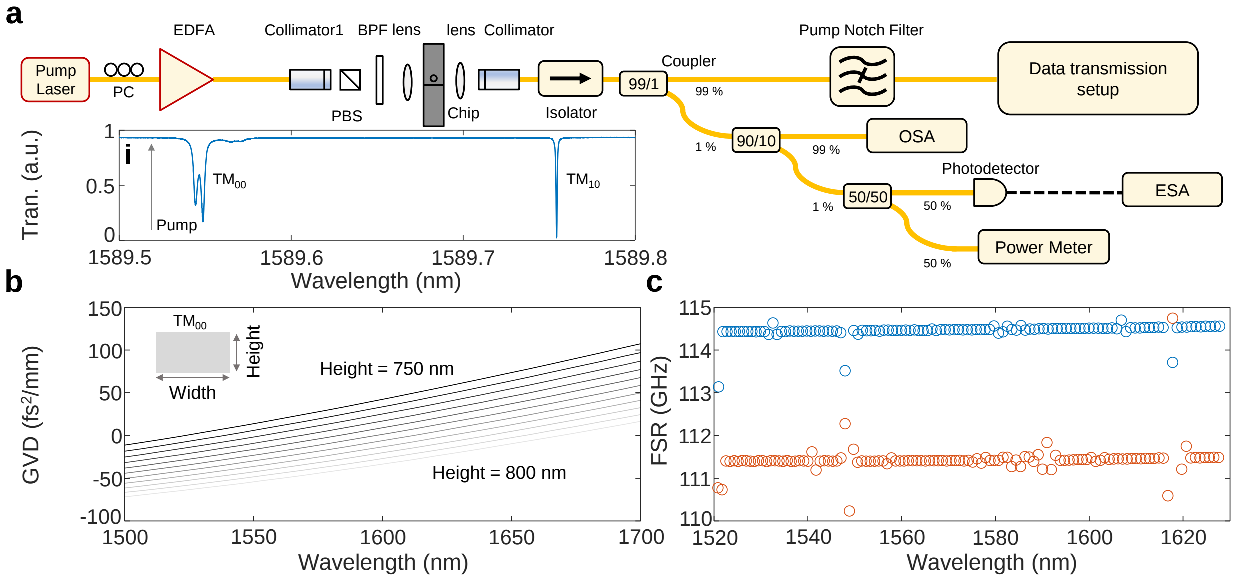

Figure S1 | Experimental setup of platicon frequency microcomb generation and the microresonator cavity mode dispersion design and characterization. a, Experimental setup of the 115 GHz platicon frequency microcomb generation and characterization. Inset **i**: the measured cavity mode spectrum with the avoided-mode crossing from transverse mode families coupling. **b**, Computed cavity mode dispersion from finite-element modeling for different waveguide heights.

The waveguide width is fixed at 2 μm, while the waveguide height varies from 750 nm to 800 nm. **c**, Free spectral range characterization for the resonances of the different transverse mode families from swept-wavelength interferometry. The two transverse mode families, TM_{00} and TM_{10} have distinct FSRs, indicating that microcomb is excited in the TM_{10} mode family.

In the data transmission path, a fiber Bragg grating (FBG) notch filter with a 0.25 nm bandwidth is implemented to suppress the pump laser up to 40 dB. Inset i shows the resonant mode spectrum including the fundamental mode (TM_{00}) and higher order mode (TM_{10}). The platicon frequency microcomb is generated by sweeping the pump wavelength from shorter wavelength to longer wavelength towards TM_{10} resonance near avoided mode crossing (AMX). The AMX facilitates the frequency microcomb generation in normal dispersion regime. Figure S1b shows the calculated group velocity dispersion (GVD) by varying the waveguide height at the fixed waveguide width to explore the fabrication height uncertainty. The waveguide height is varied from 750 to 800 nm while the width is fixed at 2 μm. Figure S1c depicts the dispersion characterization of the designed microresonator. Through a high resolution swept-wavelength-interferometry (SWI) and mode family identification processes, two TM mode families are identified, with FSRs of 111.5 GHz and 114.5 GHz, respectively. The 115 GHz microcomb line frequency spacing confirms that the microcomb is generated in the TM_{10} mode family. Second-order polynomial fitting is applied for both mode families to extract the GVD and third-order dispersion (TOD). The fitting results show that the TM_{00} mode family with $D_2/2\pi$ = - 310 kHz and $D_3/2\pi$ = 8.6 kHz, and the TM_{10} mode family with $D_2/2\pi$ = - 428 kHz and $D_3/2\pi$ = 6 kHz. Both mode families have normal GVD. By comparing the measured and calculated dispersion, we can pinpoint that our normal-dispersion microresonator has $\approx 2 \times 0.75$ μm^2 cross-section with an ≈ 6% thickness or waveguide width uncertainty. Insets are the calculated E_y-field mode profiles from finite-element computation for a waveguide cross-section of 2×0.75 μm^2. Figure S2 shows the experimental results for the Platicon frequency microcomb and the corresponding ultrafast measurement for examining the mode-locking property.

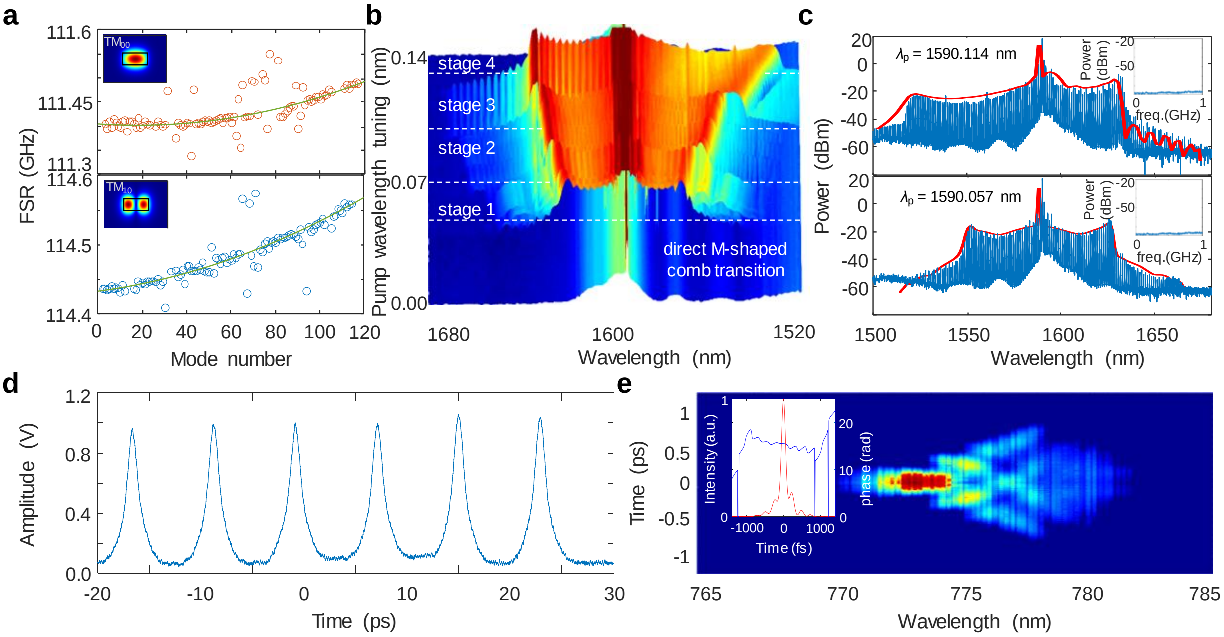

Figure S2 | Broadband platicon frequency microcombs and coherent mode-locked pulse generation metrology. a, Polynomial curve fitting over the C/L bands for two TM mode resonance families. The polynomial fitting for the TM_{00} mode family in the upper panel results in $D_2/2\pi$ = - 310 kHz and $D_3/2\pi$ = 8.6 kHz, indicating normal dispersion. The lower panel shows the TM_{10} mode family with fitted $D_2/2\pi$ = - 428 kHz, and $D_3/2\pi$ = 6 kHz, indicating normal dispersion as well. Insets show the corresponding calculated mode profiles. The distinct FSR confirms that the platicon microcomb is generated in the TM_{10} mode family. **b,** The optical spectral evolution of the platicon microcomb. The comb spectral width increases stepwise as the detuning progresses. Stage 1 represents the primary comb line stage, while stages 2–4 correspond to platicon microcomb states with asymmetric optical spectral profiles. **c,** Two representative comb spectra in states 2 and 4, respectively. Right insets: intensity noise measurements indicate low noise comb in both stages. An example of the detector noise limit is shown in red in the subpanels. **d,** Second-harmonic autocorrelation measurement of the platicon frequency microcomb, indicating sub-picosecond platicon pulse generation. **e,** Second-harmonic frequency-resolved optical gating measurement of the platicon microcomb pulse. Inset: retrieved temporal profile with phase information from the reconstructed 2D profile using a generic algorithm.

The Figure S3 depicts the platicon frequency microcomb dynamics depending on the pump-resonance detuning. Figure S3a and S3b present the simulated and measured optical spectra. The microcomb starts from primary comb lines with 5-FSR away from the pump, then transit into a breathing state with breathing frequency of 400 MHz, then evolves into low noise states. With forward tuning of the laser wavelength, the microcomb remains low intensity noise, with increasing comb bandwidth. Figure S3c shows the measured intensity noise power spectrum corresponding to the microcomb states in the Figure S3b. Note that in the current microcomb evolution dynamics, no high noise states are observed in the simulation and experiment. When the AMX frequency shift is large enough, high noise state will start to occur. We note that for our data transmission measurements, the Platicon microcomb low-noise state is stable for at least five to ten hours, without any active feedback control or additional mechanisms. Only a high-precision temperature controller is needed to stabilize the chip and microring temperature.

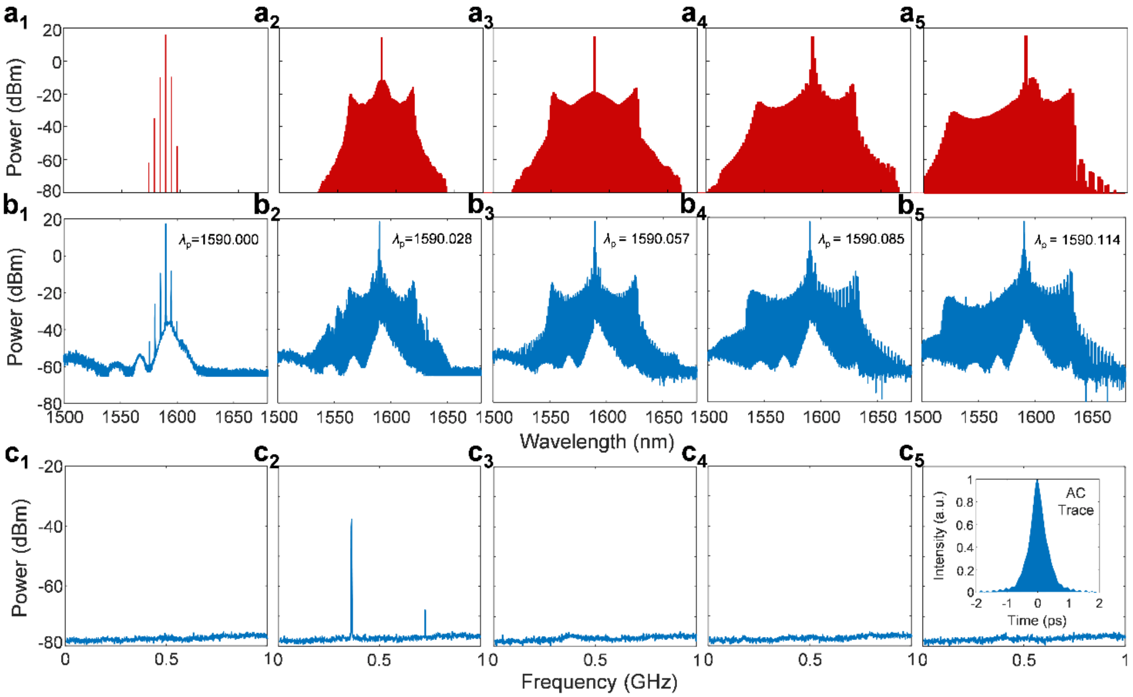

Figure S3 | Broadband platicon frequency microcomb and coherent mode-locked pulse generation metrology. a, Modeled platicon frequency microcomb at different pump-resonance detunings through the Lugiato-Lefever equation, starting from the primary microcomb lines aided by the avoided-mode crossing to platicon frequency microcomb, with the tunable optical bandwidth and different spectral asymmetry. **b,** Corresponding measured platicon frequency microcomb at the different pump-resonance detunings where the measurements agree well with the modeling. **c,** Intensity noise of the generated platicon mode-locked pulse.

Figure S4 depicts the different simulated Platicon frequency microcomb evolution dynamics with the high noise and breathing state. Figure S4a depicts the 2D spectral evolution and Figure S1b shows the total microcomb power with respect to pump-resonance detuning, from which we identify different comb states. In this simulation, the AMX frequency shift is set at 720 MHz, while the remaining parameters are set at the same in the method section of main text. In this evolution, the microcomb starts from primary comb line of 4-FSR away from the pump, then transits into high noise state, and later accesses a breathing state. Eventually it transits into a low noise state with extending comb bandwidth as the detuning increases. Figure S4c and S4d are the selected optical spectral and temporal profiles, respectively, depicting the four comb states discussed above.

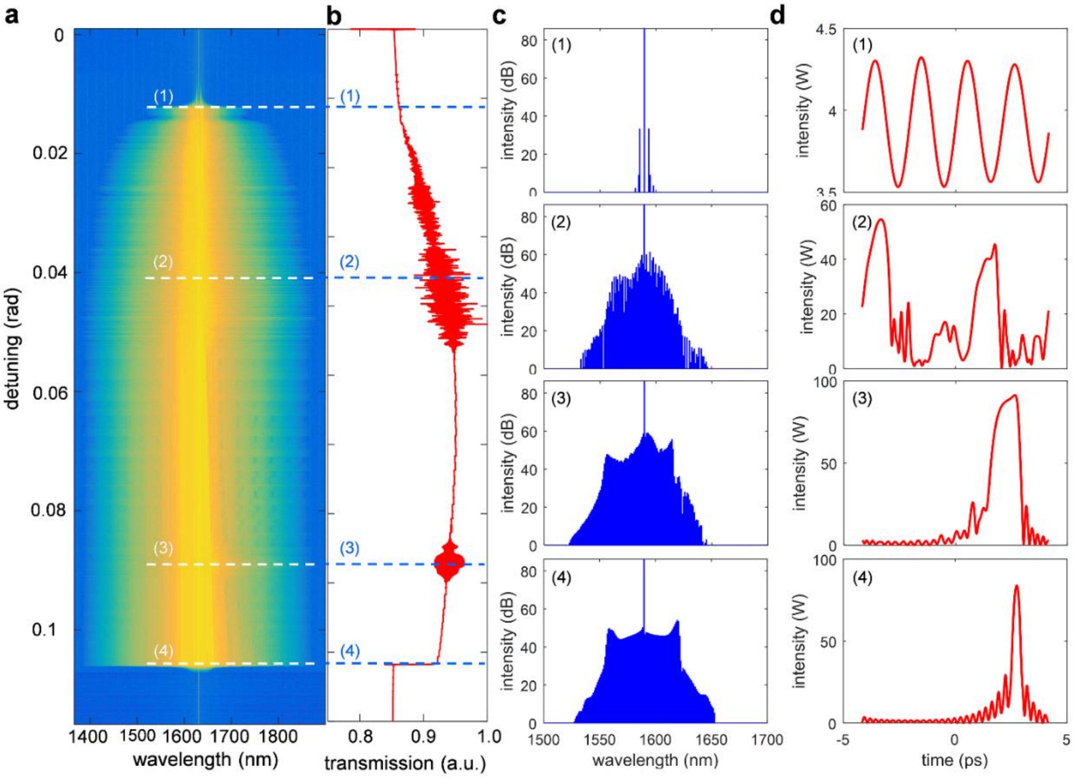

Figure S4 | The simulated Platicon frequency microcomb dynamics when the avoided mode frequency shift is larger. **a**, The simulated optical spectral evolution with respect to the pump-resonance detuning. **b**, Total microcomb power. **c**, The representatively optical spectral microcomb spectra. **d**, The temporal profiles corresponding to **c**.

During the chip design process, we selectively choose the optimal coupling strength (or mode interaction) to achieve efficient platicon generation and a broader optical spectrum bandwidth. The effect of varying mode interaction strengths is simulated in Figure S5 to optimize the spectral characteristics.

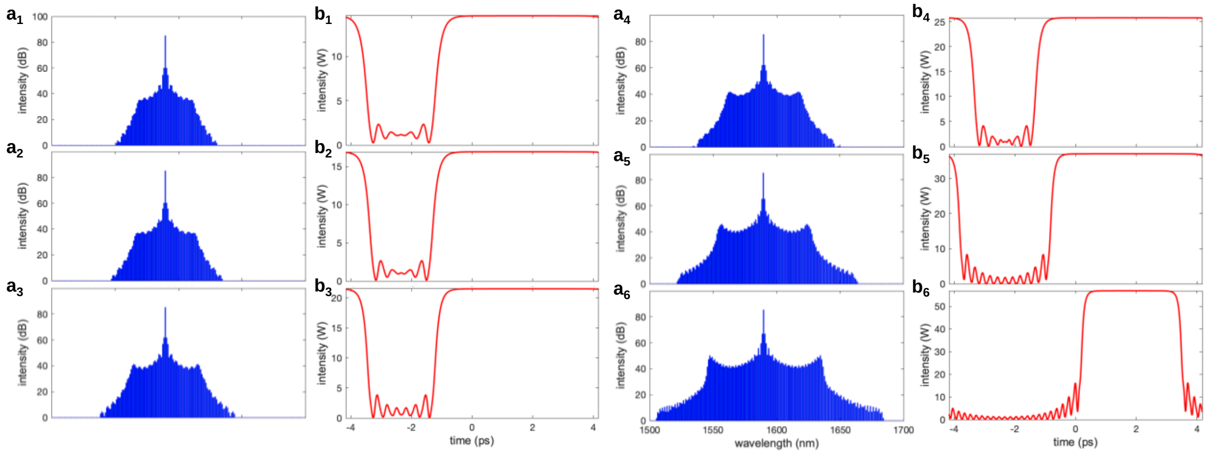

Figure S5 | The platicon states in frequency and fast time by simulation. a_1-a_6 show the platicon states corresponding to the AMX strength at 400 MHz, 350 MHz, 300 MHz, 250 MHz, 200 MHz, and 150 MHz, respectively. **b_1-b_6** The corresponding fast-time pulses with the AMX strength above.

II. The free-space WDM fronthaul coherent optical communication

The data transmission setup is illustrated in the Figure S6a with the related DSP scheme for transmitter and receiver. In the transmitter, the multi-level QAM signaling, pulse shaping, and frequency response pre-compensation are carried out to enhance the tolerance to noise impairments in our communication system. In the receiver side, the matched filtering, clock recovering, polarization demultiplexing, carrier phase estimating, delay compensating, symbol comparing, IQ separating, and error bit counting are performed to examine the quality of the data transmission. Figure S6b shows the recovered beat note spectra where linewidth is determined by the local oscillator and the Platicon frequency microcomb linewidth over all of the data transmission channels.

The single carrier fronthaul data transmission experiment is carried out based on the setup shown in Figure S6. The individual comb lines are selected for multiple-purpose data transmission. The selected comb lines can be modulated with different modulation formats and different data rate and deliver to the different locations. The fronthaul data transmission is performed at the L-band and it can be easily expanded into the C-band and U-band for more access points and more purposes. Bottom right inset shows the selected individual comb lines for multiple-access wireless networks which show the gradually optical power decrease around 19 dB. The corresponding OSNR of each comb line is shown in Figure S8b at the receiver side, extracted from Figure S8a inset. The absolute 1% optical power of each comb line after a 99:1 optical coupler before injection into a coherent receiver (extracted from Figure S8a inset) is denoted in Figure S8c.

The recovered beat note spectra show narrow linewidth characteristic which in turn demonstrate the low noise performance of the platicon frequency microcomb. By utilizing amplitude compensation algorithm [S1], amplitude noise induced by free-space data transmission link is compensated. Figure S6c and S6d show bit error rate distribution and constellation before and after amplitude noise compensation. The PRBS bit sequences are generated to synthesize the PM-16QAM symbol sequences, which are used to modulate the microcomb carriers after raised-cosine (RC) phase shaping with a roll-off factor of 0.5 over a convolution length of 21 symbols 99 taps and digital-to-analog conversion (DAC). Then, the noise loading measurement is carried out to qualify noise performance of microcomb lines as shown in Figure S7a. By alternately decreasing and increasing signal power and noise power respectively, OSNR of the received optical signal can be gradually decreased, with higher BER and worse constellation diagram [S2]. Inset shows the retrieved constellation diagrams of the ECDL and comb line at 1561.32 nm for the X and Y polarizations with corresponding BERs. Based on the reconstructed constellation diagrams, the microcomb comb line does show extra phase and intensity noise. Figure S7b and S7c show the measured optical spectra of the selected platicon frequency microcomb line and reference laser with different loading noise power.

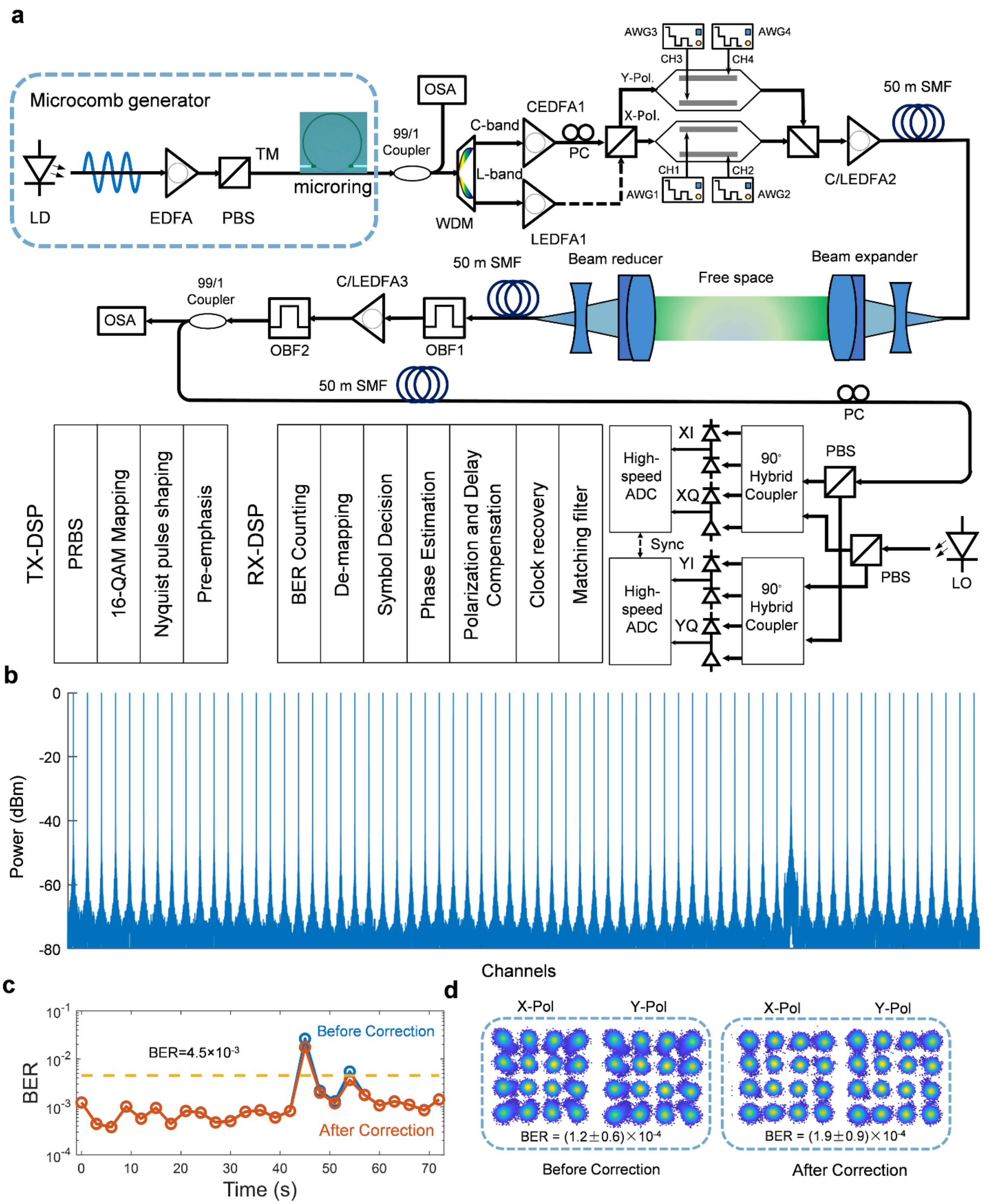

Figure S6 | Coherent WDM data transmission. a, Data transmission setup and associated DSP scheme. LD: laser diode, EDFA: erbium-doped fiber amplifier, PBS: polarization beam splitter, OSA: optical spectral analyzer, WDM: wavelength division multiplexing, CEDFA: C-band EDFA, LEDFA: L-band EDFA, AWG: arbitrary waveform generation, SMF: single-mode fiber, TX-DSP:

transmitter digital signal processing, OBF: optical bandpass filter, PC: polarization controller, LO: local oscillator, XI: X-polarization in-phase component, XQ: X-polarization quadrature component, YI: Y-polarization in-phase component, YQ: Y-polarization quadrature component, ADC: analog-to-digital converter, TX-DSP: transmitter digital signal processing, RX-DSP: receiver digital signal processing, and PRBS: Pseudo-random bit sequence. **b**, The beat note spectra of each optical carrier channels over C-band and L-band spectral ranges. **c** and **d**, The bit error rate and constellation before and after amplitude noise compensation.

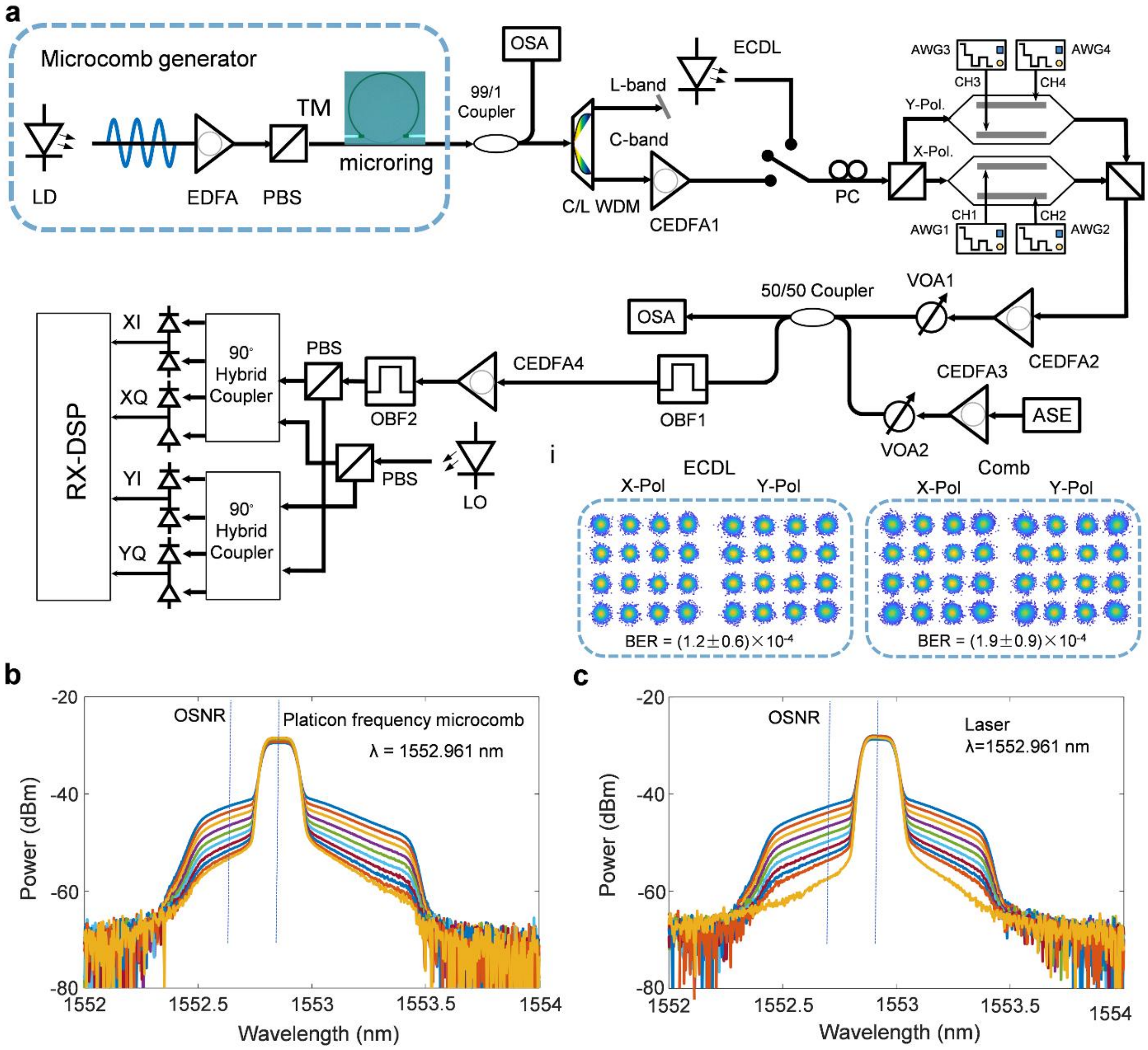

Figure S7 | Noise loading setup and associated baseband spectrum after a serial DSP. a, Noise loading setup for examining the Platicon frequency microcomb line noise property compared to the standalone ECDL. Inset **i**: Retrieved constellation diagrams of the ECDL and the comb line at

1561.32 nm for the X-polarization and Y-polarization with the corresponding BER. **b** and **c**, The measured optical spectra of the selected microcomb line and reference laser.

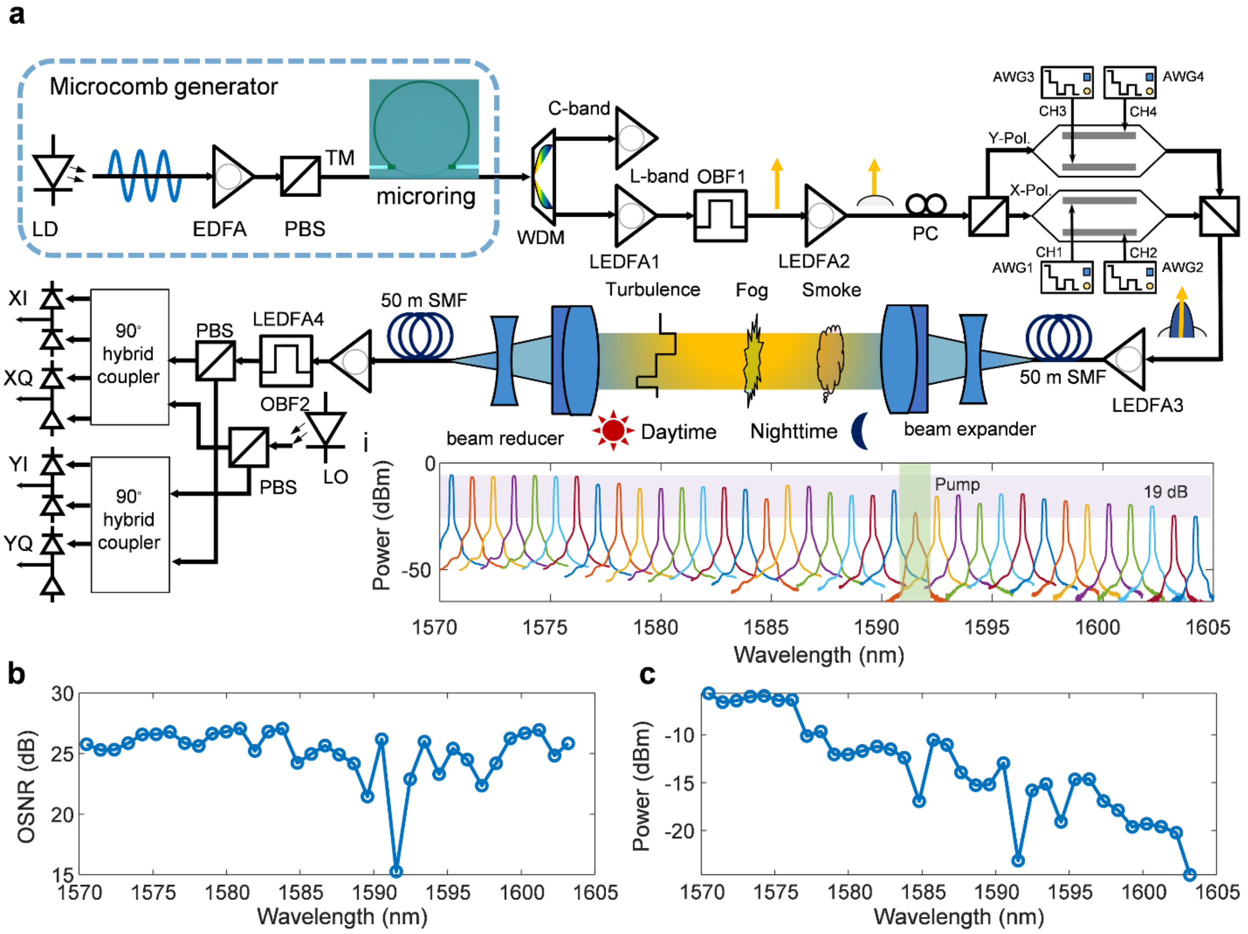

Figure S8 | Coherent free-space fronthaul data transmission over a 160 m horizontal free-space link. a, Experimental setup for the fronthaul link for wireless access network. Bottom right inset: selected individual comb lines for multiple-access wireless networks. **b**, Corresponding optical signal-to-noise ratio (OSNR) of each comb lines at the receiver side. **c**, Absolute 1% optical power of each comb lines after a 99:1 optical coupler before injecting into a coherent receiver.

The frequency microcomb lines should be aligned to ITU-T spectral grid. The frequency mismatch between them is defined as $v_n - v_n' = \Delta v_0 + n\Delta f_r$, where including both absolute offset frequency mismatch and frequency spacing mismatching, v_0 is the central comb line frequency, f_r is the repetition rate, *n* is an integer number counting the comb lines from the central frequency. This is illustrated in Figure S9. The maximum frequency mismatch is limited by the 3-dB bandwidth of the WDM channel. Due to the large WDM channel bandwidth such as 24 GHz for 100 GHz WDM, when the central frequencies are aligned, the frequency mismatch percentage is up to 24 %. Fortunately, the microcomb line-by-line resonances can be tuned thermally – as examined prior in the fiber-links [S3] – at approximately -2.2 GHz/K to -2.7 GHz/K optical carrier control. Subsequently the free spectral range between carriers, to attempt to match the ITU-T grid, can be thermally tuned post-fabrication with approximately 40 MHz range and 200 kHz precision. Tight fabrication control is certainly needed to tune the free spectral range close to the ITU-T grid first, and subsequently with thermal post-fabrication tuning.

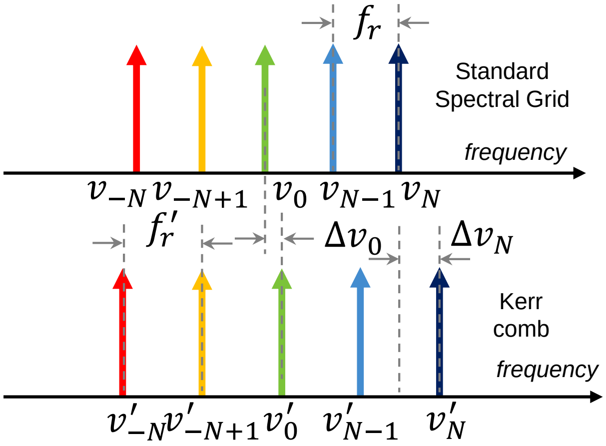

Figure S9 | Schematic of frequency mismatch between frequency microcomb lines and standard spectral grid.

III. Optical free-space link design and characterization

Several channel fading effects in the atmospheric turbulent free-space link affect received optical power and finally degrade SNR at the receiver. Here we take the constant attenuations (e.g., fog and smoke) and variable fading (e.g., atmospheric turbulence and pointing error) into account.

III.A. Optical free-space link

The free-space link setup is denoted in Figure S10 which includes two beam expanders, steering mirrors and an active feedback control system. Different collimators are used for the transmitter and receiver to avoid spurious reflections in the link optical signal. To examine the data transmission quality, a flat folding mirror is placed in the building II. Subsequently, the impact of the atmospheric turbulence on the wavefront of the laser beam during propagation is considered through inserting a series of equally distributed phase screen in beam propagation theory. In our simulation, the light propagates along *z*-direction and the random phase plane resides in the *xy*-plane. The complex amplitude of the laser beam after the amplitude and phase distortion can be denoted as [S4, S5].

$$U(\mathrm{x,y}) = \mathrm{FFT}^{-1}\big[\mathrm{FFT}[U_0(x,y)]U\big(k_x,k_y\big)\big]\exp\,[iFFT[(C \times (2\pi)^3 (k_x^2+k_y^2)\Delta z\ \times 0.033 C_n^2 \Bigg(1 + 1.802\sqrt{\frac{k_x^2+k_y^2}{k_l^2}} - 0.254\left(\frac{k_x^2+k_y^2}{k_l^2}\right)^{-7/12}\Bigg) exp\left[\frac{k_x^2+k_y^2}{k_l^2}\right]\left(k_x^2+k_y^2+\frac{1}{L_0^2}\right)^{-11/6})^{0.5}]] \tag{S1}$$

where $U_0(x,y) = \sqrt{\frac{2I_0}{\pi\omega^2}} exp\left[-\frac{x^2+y^2}{\omega^2}\right]$ is the amplitude of the laser beam, $U\big(k_x,k_y\big) = \exp\,[i\Delta z\sqrt{\big(k^2-k_x^2-k_y^2\big)}]$ is the phase delay, I_0 is the light intensity, Δz is the propagation distance, k_x and k_y are the *x*-axis and *y*-axis wavenumbers, $\omega(z) = z\left[1+\left(\frac{\pi\omega_0^2}{\lambda L}\right)^2\right]$, ω_0 the initial Gaussian laser beam waist, C is the complex random numbers with a mean of zero and variance of one, and *L* is the propagation distance. To investigate the impact of atmospheric turbulence on the Gaussian beam, we simulate the random phase plane and assume the light is propagating between the adjacent phase planes. We get the wavefront at different position along with the propagation direction *z* to visualize the optical power distribution at the wavefront. The calculated Gaussian beam wavefront is shown in inset when *z* = 60 m after considering the atmospheric turbulence with the experimentally measured C_n^2.

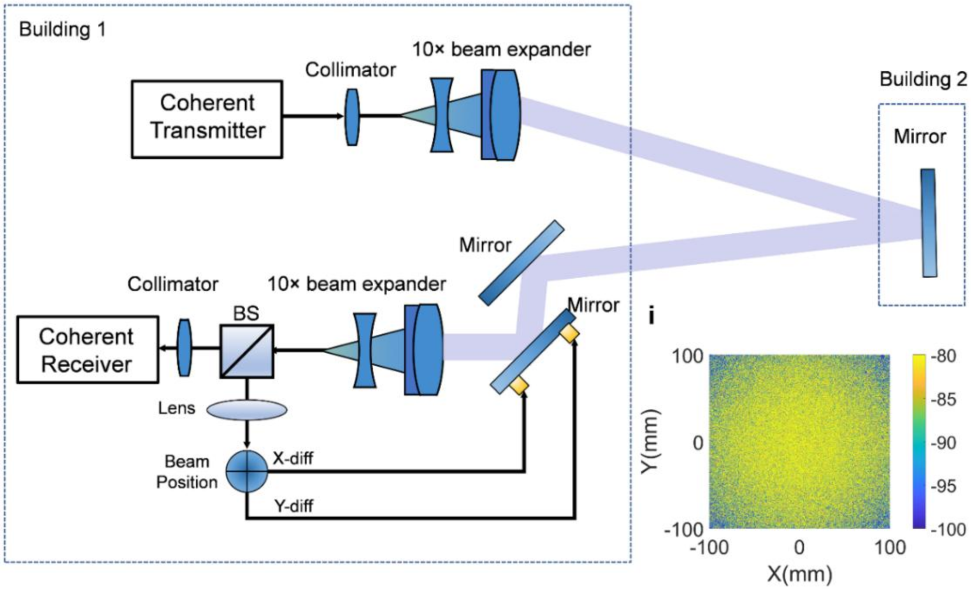

Figure S10 | Free-space link setup and wavefront during the propagation. Free-space atmospheric link setup. Inset: modeled optical Gaussian beam wavefront using measured C_n^2.

III.B. Optical free-space communication channel model

We utilize 16-QAM electrical data streams to modulate the optical carriers leading to the optical intensity at the transmitter output as [S6]:

$$\mathrm{e}(t) = \mathrm{P}\left\{1 + \alpha\left[e_I(t)cos(2\pi f_c t) - e_Q(t)sin(2\pi f_c t)\right]\right\} \tag{S2}$$

where P is transmitted optical power, $e_I(t) = \sum_{i=-\infty}^{\infty} a_i f(t - it_s)$ and $e_Q(t) = \sum_{i=-\infty}^{\infty} b_i f(t - it_s)$ are the in-phase and the quadrature bit sequences respectively, a_i and b_i are the in-phase and quadrature amplitude of the i_{th} complex symbol, $f(t)$ is the shaping function, t_s is the symbol duration, and $0 < \alpha \leq 1$ is the modulation depth. Due to propagation impairments including geometrical loss induced by beam divergence, channel atmospheric loss, and background radiation, and random processes for the signal scintillation caused by environment variations, atmospheric turbulence, and pointing error, the received signal will be impaired as

$$P_o(t) = \alpha_f X(t) P\left\{1 + \alpha\left[e_I(t)cos(2\pi f_c t) - e_Q(t)sin(2\pi f_c t)\right]\right\} \tag{S3}$$

where α_f is the free-space link loss, $X(t)$ is the random impairment which is the time dependent random variable following a log-normal distribution for the weak atmospheric turbulence, random power distribution for the non-zero boresight pointing error, and random power distribution for the fog-smoke channel. The telescope at the receiver side narrows the laser beam which is coupled into a balanced high-speed PIN photodetector via a single mode fiber. After optical-electrical conversion, the electrical signal at the output of the PIN photodetector is

$$P_e(t) = GR\alpha_f X(t)\left\{\alpha\left[e_I(t)cos(2\pi f_c t) - e_Q(t)sin(2\pi f_c t)\right]\right\} + N_{sh}(t) + N_{Th}(t) \tag{S4}$$

where G is the transimpedance gain, R is the detector responsivity, $N_{sh}(t) = 2qGFRx\alpha_f \alpha P\Delta f$ and $N_{Th}(t) = \left(4k_B \frac{T}{R_L}\right) F_n \Delta f$ are the photoreceiver shot noise and thermal noise. x, q, F, Δf denote respectively the instantaneous fading sample, electron charge, the excess noise factor of PIN detector, the symbol noise bandwidth. k_B, T, R_L, and F_n are respectively the Boltzmann constant, the PIN receiver's temperature, load resistance, and the noise figure.

The bit error rate of the atmospheric free-space link can be modeled as a slow-fading channel which is described with a general equation as [S7]

$$\mathrm{BER} = \int_0^{\infty} BER_{inst} f_X(x)dx \tag{S5}$$

For the $M_I \times M_Q$ QAM, the system BER can be described with

$$\mathrm{BER} = \frac{1}{log_2(M_I M_Q)}\left(P_I + P_Q\right) \tag{S6}$$

where

$$P_I = \sum_{k=1}^{log_2 M_I} \int_0^{\infty} P_{M_I}(k) f_X(x) dx \tag{S7}$$

$$P_Q = \sum_{l=1}^{log_2 M_Q} \int_0^{\infty} P_{M_Q}(l) f_X(x) dx \tag{S8}$$

where

$$P_{M_I}(k) = \frac{1}{M_I} \sum_{i=0}^{(1-2^{-k})M_I - 1} \left\{ \begin{array}{c} (-1)^{\left[\frac{i \cdot 2^{k-1}}{M_I}\right]} \left(2^{k-1} - \left[\frac{i \cdot 2^{k-1}}{M_I} + \frac{1}{2}\right]\right) \\ \times erfc\left((2i+1) \sqrt{\frac{3\gamma}{2\left(\left(M_I^2 - 1\right) + \vartheta^2 \left(M_Q^2 - 1\right)\right)}} \right) \end{array} \right\} \tag{S9}$$

$$P_{M_Q}(l) = \frac{1}{M_Q} \sum_{j=0}^{(1-2^{-l})M_Q - 1} \left\{ \begin{array}{c} (-1)^{\left[\frac{j \cdot 2^{l-1}}{M_Q}\right]} \left(2^{l-1} - \left[\frac{j \cdot 2^{l-1}}{M_Q} + \frac{1}{2}\right]\right) \\ \times erfc\left((2j+1) \sqrt{\frac{3\vartheta^2\gamma}{2\left(\left(M_I^2 - 1\right) + \vartheta^2 \left(M_Q^2 - 1\right)\right)}} \right) \end{array} \right\} \tag{S10}$$

where $\gamma = \frac{\left(GRx\alpha_f P\right)^2}{N_{sh}(t) + N_{Th}(t)}$ is the instantaneous electrical signal to noise ratio per symbol, $\vartheta = d_Q / d_I$ is the quadrature-to-inphase decision distance ratio. Due to the laser beam propagation over the atmospheric free-space channel, the amplitude and phase of the optical signal are impaired by various atmospheric interferences. Here we mainly consider the perturbation factors including the atmospheric attenuation including non-zero boresight pointing error, weak atmospheric turbulence, and fog and smoke. The weak atmospheric turbulence can be described by the log-normal distribution, where the probability density function (PDF) $f_X(x)$ can be written as [S7]

$$f_{X-LN}(x) = \frac{1}{x\sigma_P\sqrt{2\pi}} e^{\frac{-\left[lnx + \frac{\sigma_P^2}{2}\right]^2}{2\sigma_P^2}} \tag{S11}$$

where σ_P^2 is the scintillation index depending on the channel's characteristics as

$$\sigma_P^2 = exp\left[\frac{0.49\sigma_R^2}{\left(1 + 0.81d^2 + 0.56\sigma_R^{12/5}\right)^{7/6}} + \frac{0.49\sigma_R^2\left(1 + 0.69\sigma_R^{12/5}\right)^{-5/6}}{\left(1 + 0.9d^2 + 0.62d^2\sigma_R^{12/5}\right)}\right] - 1 \tag{S12}$$

with $d = \sqrt{kD^2/4L}$ depending on the link distance L and aperture diameter of receiver D. $k = 2\pi/\lambda$ is the optical wave number. $\sigma_R^2 = 0.492 C_n^2 k^{7/6} L^{11/6}$ is the Rytov variance in the case of spherical wave propagation. The analytical expression of the P_I and P_Q after considering the Gauss-Hermite quadrature integration can be expressed as

$$P_I \approx \sum_{k=1}^{log_2 M_I} \sum_{i=0}^{(1-2^{-k})M_I-1} \sum_{t=-N;t\neq 0}^{N} A_i \frac{1}{\sqrt{\pi}} \times \omega_t erfc\left(B_i \sqrt{\frac{a\times exp\left(2\sqrt{2}\sigma_P\mu_t-\sigma_P^2\right)}{b\times exp\left(2\sqrt{2}\sigma_P\mu_t-\sigma_P^2/2\right)+N_{th}}}\right) \quad \text{(S13)}$$

$$P_Q \approx \sum_{l=1}^{log_2 M_Q} \sum_{j=0}^{(1-l)M_Q-1} \sum_{t=-N;t\neq 0}^{N} A_j \frac{1}{\sqrt{\pi}} \times \omega_t erfc\left(B_j \sqrt{\frac{a\times exp\left(2\sqrt{2}\sigma_P\mu_t-\sigma_P^2\right)}{b\times exp\left(2\sqrt{2}\sigma_P\mu_t-\sigma_P^2/2\right)+N_{th}}}\right) \quad \text{(S14)}$$

where $A_i = \frac{1}{M_I}(-1)^{\left[\frac{i\cdot 2^{k-1}}{M_I}\right]}\left(2^{k-1} - \left[\frac{i\cdot 2^{k-1}}{M_I} + \frac{1}{2}\right]\right)$, $A_j = \frac{1}{M_Q}(-1)^{\left[\frac{j\cdot 2^{l-1}}{M_Q}\right]}\left(2^{l-1} - \left[\frac{j\cdot 2^{l-1}}{M_Q} + \frac{1}{2}\right]\right)$, $B_i = (2\mathrm{i}+1)\sqrt{3/\left(2\left((M_I^2-1)+\vartheta^2\left(M_Q^2-1\right)\right)\right)}$, $B_j = (2\mathrm{j}+1)\sqrt{3/\left(2\left((M_I^2-1)+\vartheta^2\left(M_Q^2-1\right)\right)\right)}$, $\mu = \left(lnx + \frac{\sigma_P^2}{2}\right)/\sqrt{2}\sigma_P$, $a = \left(GR\alpha_f P\right)^2$, $b = 2qGFR\alpha_f \alpha P\Delta f$, ω_t and μ_t represent the weight factors and the zeros of the Hermite polynomial with respect to $t = (-N, -N+1, \ldots, 1, 2, \ldots, N)$. Moreover, we considered the effect of the fog or smoke channel on the bit error rate based on the Kim model [50], where the q parameter is defined as:

$$q = \begin{cases} 1.6, & Vis > 50 \\ 1.3, & 6 < Vis < 50 \\ 0.16 \times Vis + 0.34, & 1 < Vis < 6 \\ Vis - 0.5, & 0.5 < Vis < 1 \\ 0, & Vis < 0.5 \end{cases} \quad \text{(S15)}$$

Based on the Beer’s lambert law, the fog or smoke channel loss can be denoted as

$$h_{FS} = \exp\left(\frac{ln0.02}{Vis}\left(\frac{\lambda}{\lambda_0}\right)^{-q} L\right) \quad \text{(S16)}$$

The optical signal to noise ratio (OSNR) in the free-space atmospheric communication system can be modeled from the given optical carrier to noise ratio (OCNR) of the frequency microcomb to the electrical signal noise ratio (SNR) through the OCNR after the pre-amplifier, the OSNR after the coherent transmitter and before the coherent receiver without considering the free-space link power fading. The difference between the optical frequency comb and the conventional laser array for the WDM system is the optical frequency comb offers the multiple optical carriers with excellent phase coherence between channels and channel spacing stability, in a single chip. The lower optical power per channel is compensated by an extra optical amplifier to amplify the optical signal power. In our case, we utilized the platicon frequency microcomb as a multiple carrier source for the WDM system. Noise of the free space communication system mainly originates from atmospheric environment, optical amplifier and photodetection. The received $\mathrm{OSNR_{RX}}$ for the point-point free-space communication link without intermediate repeaters can be described with [S8, S9]

$$OSNR_{RX} = \frac{G_{pre3} g_1 G_{pre2} g_0 G_{pre1} P_{low}}{G_{pre3} g_1 \left(G_{pre2} \left(\frac{g_0}{2} \left(G_{pre1} N_0 \Delta v + F_{pre1} h v \Delta v \left(G_{pre1} - 1 \right) \right) \right) + F_{pre2} h v \Delta v \left(G_{pre2} - 1 \right) \right) + F_{pre_3} h v \Delta v \left(G_{pre3} - 1 \right)} \quad \text{(S17)}$$

where $P_{low} = P_{noise}/OCNR$ is the lowest power of all comb lines, G_{pre} is the gain of the pre-amplifier, F_{pre} is the noise figure of the preamplifier, hv is the photon energy, Δv is the reference bandwidth, g_0 and g_1 are the power attenuation from the PDM IQ modulator and free-space channel. The OSNR is defined as the ratio of the signal power to the noise power within a reference bandwidth.

After considering the free-space link power fading, the received $\mathrm{OSNR_{RX}}$ is given by P_R/N_R, where P_R is the average output of EDFA3 and N_R is the optical noise intensity after EDFA3. The input of EDFA3 can be roughly given by $x(t)GP_{line}$, where x is the fading term attributed to atmospheric scenarios and G is the gain factor at the transmitter side. Thus the optical noise intensity N_R after EDFA3 can be expressed as $N_R = P_R/OSNR_{TX} + 2\pi n_{sp} \hbar v B_{ref} [P_R/(\bar{x} P_{line} G) - 1]$. Therefore, different atmospheric scenarios affect the instantaneous $\mathrm{OSNR_{RX}}$ by introducing the average intensity fading $\bar{x}$, along with the subsequent ASE noise when compensating the free-space link loss.

With the measured link parameters on-hand, Figure S11a shows the dependence of the calculated theoretical 16-QAM SER on the SNR for different channel fading models: ideal channel, low visibility fog and smoke channel (F&S channel), atmospheric turbulence (AT) log-normal channel, and non-zero boresight PE channel. The symbol error probability of M-QAM is denoted as $\mathrm{SER} = 2(1 - \frac{1}{\sqrt{M}}) erfc(k\sqrt{\mathrm{SNR}})$ where $k = \sqrt{\frac{3}{2(M-1)}}$ is the normalizing factor for different M-ary QAM. Adverse channel fading fundamentally limits the transmission reach of the free-space link. The average SER influenced by intensity scintillation of the free-space link is defined with $\mathrm{SER}_{FS} = \int_0^{\infty} \mathrm{SER} f_I(x)\, dx$, where x denotes the fractional power variation and $f_I(x)$ is the power density function of the random scintillation [S10]. Atmospheric attenuation is calculated using the Beer-Lambert relation $f_I(x) = f_{FS} = e^{-\alpha_\lambda L}$, where L is the link distance and attenuation coefficient $\alpha_\lambda = -ln 0.02/Vis\,(\lambda/550)^{-q}$ is related to the atmospheric visibility [S11] with Vis and q the atmospheric visibility parameters. The intensity scintillation of the experimental free-space link can be described by a log-normal distribution denoted as $f_I(x) = f_{LN}(x) = 1/\left(x2\sigma_I\sqrt{2\pi}\right) exp\left(-\left[lnx + \frac{2\sigma_I^2}{2}\right]^2/8\sigma_I^2\right)$ [S14].

In a terrestrial free-space optical link, the light beam jitter variance along the horizontal and elevation axes are assumed to be identical, caused by the building motion and individual transmitter-receiver mechanical vibration. The non-zero boresight pointing error power density function is used to model the PE channel fading, defined as $f_I(x) = f_{PE}(x) = \gamma^2/A_0^{\gamma^2}\, x^{\gamma^2-1}$ where $0 \le x \le A_0$, and A_0 (≅ 1) is the fraction of the collected power when pointing error $r = 0$, and where $\gamma = \omega_{eq}/2\sigma_r$ (≅ 0.874) is the ratio between the equivalent beam waist ω_{eq} and the PE displacement standard deviation σ_r at the receiver [S12]. The Gaussian beam waist propagating in atmospheric turbulence can be denoted as $\omega_z \approx \omega_0\sqrt{1 + \varepsilon(\lambda z/\pi\omega_0^2)^2}$ where ω_0 is the beam waist at the transmitter for $z = 0$, $\varepsilon = (1 + 2\omega_0^2/\rho_0^2(z))$, and $\rho_0(z) = (0.55C_n^2k^2z)^{-3/5}$ as the spatial coherence length. For a circular detection aperture with radius a and Gaussian beam propagation, the equivalent beam width is expressed as $\omega_{eq} = \omega_z^2\,\sqrt{\pi}erf(h)/\left(2he^{-h^2}\right)$ where $h = \left(\sqrt{\pi}a\right)/\left(\sqrt{2}\omega_z\right)$. The subsequent SER-SNR dependence of the free-space link with different reach ranges of 160 m, 500 m, 1 km, and 10 km are plotted in Figure S11a, based on the different channel fading models.

Figure S11a shows our experimental testbed measurements with the circle symbols to compare with the modelled SER-SNR dependences. The measured SER follows the aggregate (F&S, AT and non-zero boresight PE) fading models well, with the worst-case SER still below the 1.8×10^{-2} error correction bound. We also note that the $\mathrm{OSNR_{TX}}$ before the coherent transmitter is determined by the comb line power of the platicon microcomb through the relation of $\mathrm{OSNR_{TX}} = GP_{line}/\left(GP_{line}/OCNR_{line} + [2\pi n_{sp}\hbar vB_{ref}(G-1)]\right)$ where P_{line} is the power level of the WDM carrier, G is the gain of the C- and L-EDFA after the C/L band WDM, n_{sp} is the spontaneous emission factor, $\hbar$ is the normalized Planck's constant, v is the carrier optical frequency, and B_{ref} is the OSA resolution bandwidth [S8, S9]. The received SNR in the PDM-WDM system is then calculated by $\mathrm{SNR} = \frac{B_{ref}}{B_s}\mathrm{OSNR_{RX}}$, where B_{S} is the symbol rate and $\mathrm{OSNR_{RX}}$ is related to the after-transmitter EDFAs noise figures and the $\mathrm{OSNR_{TX}}$.

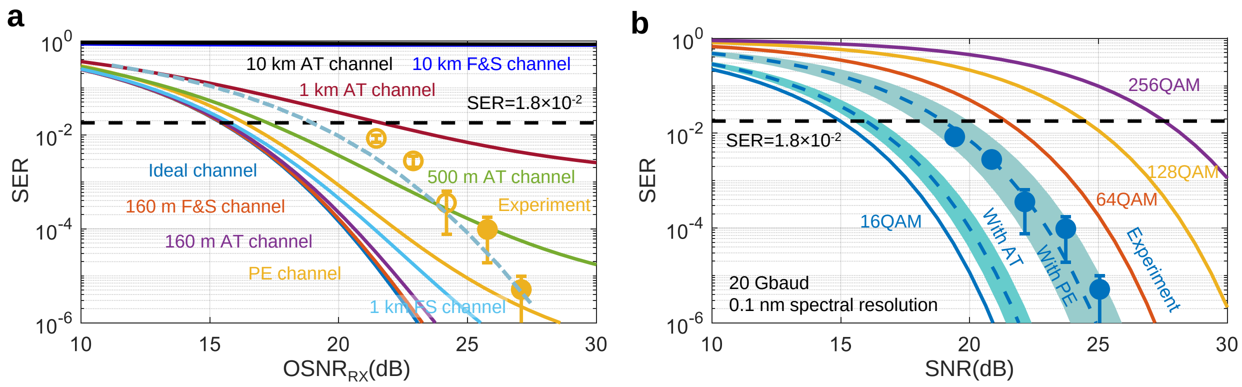

Figure S11 | a, Modeled symbol error rate (SER) – signal-to-noise ratio (SNR) of the free-space link for different channel models and scaled reach range (F&S: fog and smoke, AT: atmospheric turbulence, PE: pointing error). Our experimental testbed data points are listed, with residual pointing error and turbulence as the primary and secondary sources of error in our microcomb free-space link demonstration. **b**, Modeled SER-SNR requirements, and scaling of the free-space link for different advanced modulation formats, signaling with 20 Gbaud each. Likewise, our testbed data points are listed with the same experimental conditions as panel **b**.

IV. Free-space optical link implementation

IV.A. Free-space optical link: power fluctuations characterization and stabilization

In the free-space atmospheric link, the random fluctuating sources include beam pointing and atmospheric refractive index fluctuations described by refractive index power spectrum [S13]. Turbulence degraded wavefronts can be simulated and compensated by pre or post detection processing [S14], ideal lossless adaptive optics including a spatial mode digital coherent receiver and a multimode pre-amplifier [S15], few mode fiber [S16] and modes diversity coherent receipt [S17]. To effectively suppress the pointing error of the free-space link and power fading induced by the atmospheric turbulence, we developed the active feedback control locking system. Figure S12a-f show the free-running scenario and the active tracking scenario with beam stabilization. Figure S12a and 12b show the weather conditions in terms of temperature and humidity for stabilized and free-running link. Figures S12c and 12d show the beam position of the received light beam along *x*- axis and *y*-axis for the free-running and stabilized cases. A quadrant positional detector (Thorlabs PDQ30C) with a 150 kHz servo bandwidth (KPA101) is used for the beam feedback stabilization. We run this in closed-loop by controlling the piezoelectric adjusters of the kinematic mirror mounts (POLARIS-K2S2P), with an active feedback control bandwidth of 1 kHz.

(The link distance is 160 m which gives a traveling time delay of ≈ 520 ns and a maximum corresponding bandwidth of 1.93 MHz.) Before beam stabilization, the *x*- and *y*-axis pixel fluctuations are respectively ± 0.697 and ± 0.553 mm (one standard deviation). With active feedback locking system, the *x*- and *y*-axis transmission beam pointing errors are suppressed respectively to ± 0.052 and ± 0.042 mm (one standard deviation).

Figures S12e and 12f show the received optical power fluctuations before and after free-space beam stabilization, respectively. Even with beam positional feedback stabilization, the received power still fluctuates by 79%, which arises from residual pointing error, turbulence, and laser intensity noise.

In our link demonstration, the beam size is expanded 10 times via an achromatic Galilean beam expander to 4 cm. Consequently, the power density of our link is about 0.004 W/cm^2, much lower than the IEC 60825 eye-safety requirements. In IEC 60825 standards, the maximum permissible exposure (MPE) – the highest power or energy density (in W/cm^2 or J/cm^2) of a light source – at 1550 nm for 0.25 seconds (human blink reflex time) is 1 J/cm^2. This corresponds to 4 W/cm^2, for negligible probability of damage.

IV.B. Atmospheric turbulence characterization and statistical analysis

After removing the pointing error with the active feedback control system, we selected a portion of received power fluctuations of the stabilized and free-running link to examine the statistical parameters in terms of the link dropout period, link availability, and turbulence power distribution [S18]. Figure S13a shows the received optical intensity fluctuations. Figure S13b shows the corresponding link power density distribution above the intensity threshold more than 0.012. When the received power falls below the detection threshold, the free-space link is unavailable leading to a dropout. Figure S13c is the probability density of link dropout before stabilization; Figure S13d is the probability density of link dropout after stabilization. Link dropout is identified when the received power is lower than a defined voltage threshold, such as 70% of the maximum voltage here. Link dropout period is defined as the accumulated time between adjacent dropouts – that is, the longer the link dropout period, the more unstable the link. Before stabilization, we can see that link dropout periods lasting up to tens of seconds is even possible. This helps illustrate Figure S13d for comparison, where almost all the dropouts are between 0.1-second to 0.8-second (Figure S13d inset is a zoom-in representation of the sample). A clear suppression of the low-frequency beam fluctuations is achieved.

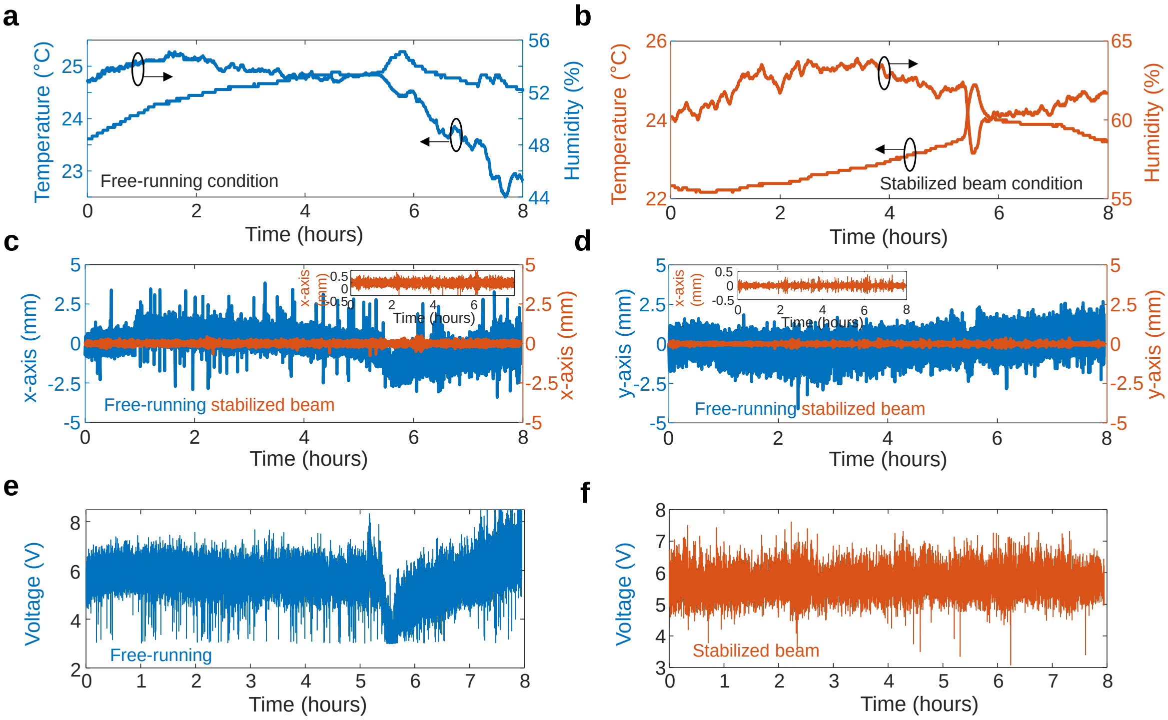

Figure S12 | Free-space link beam stabilization. a and **b**, Weather condition for the stabilized and free-running link. **c** and **d**, Beam position distribution along *x*-axis and *y*-axis before and after beam stabilization respectively. Insets: amplitude zoom-in, after beam stabilization. **e** and **f**, Received optical power fluctuations before and after free-space beam stabilization.

Figure S13e and S13f are corresponding power probability distribution density for the free-running and stabilized link respectively. The link availability shows the percentage of time per minute that the free-space link is available. The link availability depends on the defined power thresholds which is the percentage of the maximum received power. When the defined power threshold is high, the link availability will be low. The link availability before and after beam stabilization is shown in Figures S13g, and S13h. After beam stabilization, the link availability will be improved around ≈ 4.5 dB.

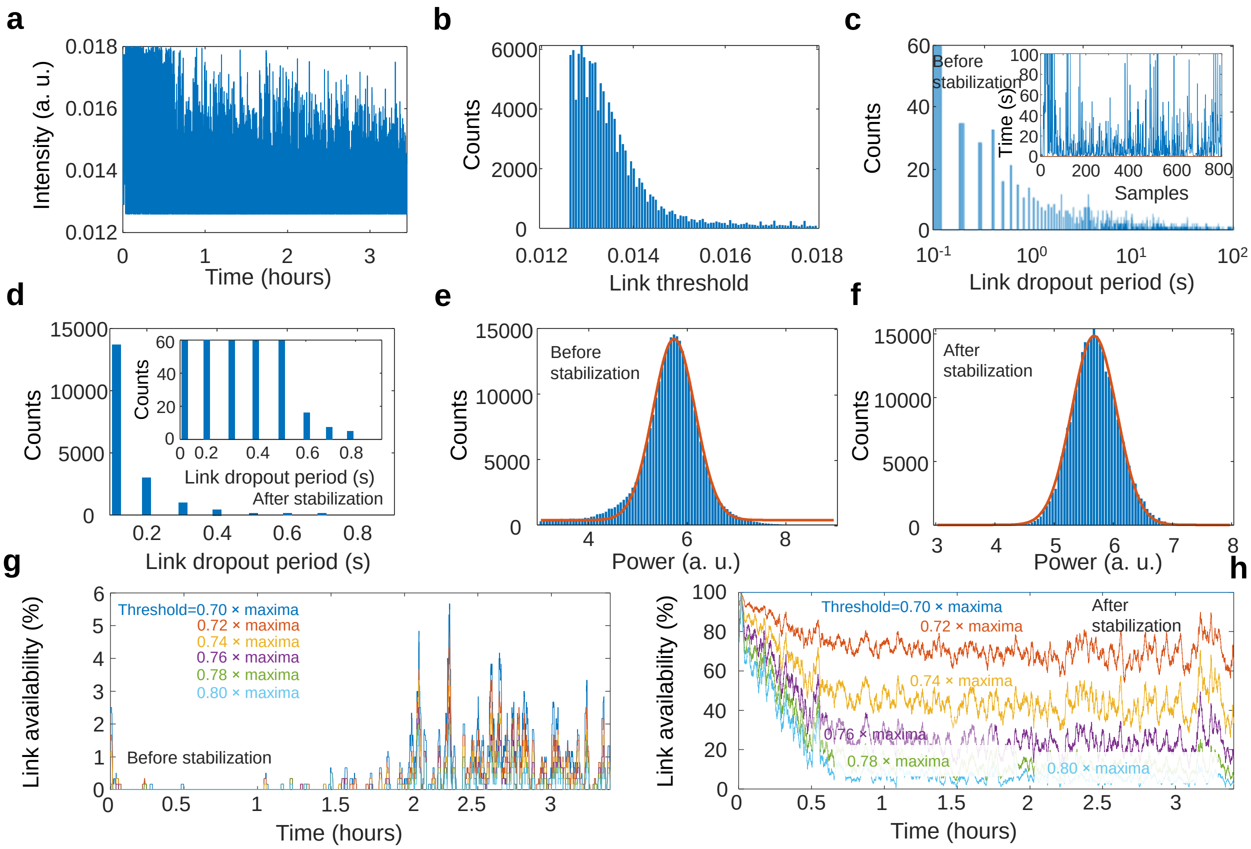

Figure S13 | Free-space link dropout time, link availability and turbulent power distribution. **a**, Optical power reception distribution. **b**, Statistical power reception probability distribution above the link threshold. **c** and **d**, Link dropout period distribution before and after beam stabilization. Inset is the zoomed view of the dropout after beam stabilization. **e** and **f**, Intensity fluctuation probability distribution of the free-running and stabilized link. **g** and **h,** The link availability before and after beam stabilization.

Supplementary References

S1. L. Li, T. Geng, Z. Wu, S. Gao, and X. Li, Design and experimental demonstration of 8-QAM coherent free-space optical communication using amplitude compensation and phase recovery. *Appl. Opt.* **60**, 5345-5353 (2021).

S2. W. Freude, R. Schmogrow, B. Nebendahl, M. Winter, A. Josten, D. Hillerkuss, S. Koenig, J. Meyer, M. Dreschmann, M. Huebner, C. Koos, J. Becker and J. Leuthold, Quality metrics for optical signals: Eye diagram, Q-factor, OSNR, EVM, and BER. *14th International conference on Transparent Optical Networks (ICTON)* (2012).

S3. P. Marin-Palomo, J. N. Kemal, M. Karpov, A. Kordts, J. Pfeifle, M. H. P. Pfeiffer, P. Trocha, S. Wolf, V. Brasch, M. H. Anderson, R. Rosenberger, K. Vijayan, W. Freude, T. J. Kippenburg, and C. Koos, Microresonator-based solitons for massively parallel coherent optical communications. *Nature* **546**, 274-279 (2017).

S4. J. D. Strasburg and W. W. Harper, Impact of atmospheric turbulence on beam propagation. *Proc. SPIE 5413*.

S5. R. Frehlich, Simulation of laser propagation in a turbulent atmosphere. *Appl. Opt.* **39**, 393-397 (2000).

S6. K. P. Peppas and C. K. Datsikas, Average symbol error probability of general-order rectangular quadrature amplitude modulation of optical wireless communication systems over atmospheric turbulence channels. *J. Opt. Commun. Netw.* **2**, 102–110 (2010).

S7. B. T. Vu, N. T. Dang, T. C. Thang, and A. T. Pham, Bit error rate analysis of rectangular QAM/FSO systems using an APD receiver over atmospheric turbulence channels. *J. Opt. Commun. Netw.* **5**, 437-446 (2013).

S8. P. Marin-Palomo, J. N. Kemal, T. J. Kippenberg, W. Freude, S. Randel, and C. Koos, Performance of chip-scale optical frequency comb generators in coherent WDM communications. *Opt. Express* **28**, 12897–12910 (2020).

S9. V. Torres-Company, J. Schröder, A. Fülöp, M. Mazur, L. Lundberg, Ó. B. Helgason, M. Karlsson, and P. A. Andrekson, Laser frequency combs for coherent optical communications. *J. Light. Technol.* **37**, 1663-1670 (2019).

S10. B. T. Vu, N. T. Dang, T. C. Thang, and A. T. Pham, Bit error rate analysis of rectangular QAM/FSO systems using an APD receiver over atmospheric turbulence channels. *J. Opt. Commun. Netw.* **5**, 437-446 (2013).

S11. M. Ijaz, Z. Ghassemlooy, J. Pesek, O. Fiser, H. Le Minh, and E. Bentley, Modeling of fog and smoke attenuation in free space optical communications link under controlled laboratory conditions. *J. Light. Technol.* **31**, 1720-1726 (2013).

S12. A. A. Farid and S. Hranilovic, Outage capacity optimization for free-space optical links with pointing errors. *J. Light. Technol.* **25**, 1702-1710 (2007).

S13. L. C. Andrews: An analytical model for the refractive index power spectrum and its application to optical scintillations in the atmosphere. *J. Mod. Opt.* **39**, 1849–1853 (1992).

S14. B. L. McGlamery: Computer simulation studies of compensation of turbulence degraded images. Image Processing, *Ed.: J. C. Urbach, SPIE* (1976), 225–233.

S15. N. K. Fontaine, R. Ryf, Y. Zhang, J. C. Alvarado-Zacarias, S. van der Heide, M. Mazur, H. Huang, H. Chen, R. Amezcua-Correa, G. Li, M. Capuzzo, R. Kopf, A. Tate, H. Safar, C. Bolle, D. T. Neilson, E. Burrows, K. Kim, M. Bigot-Astruc, F. Achten, P. Sillard, A. Amezcua-Correa, and J. Carpenter, Digital turbulence compensation of free space optical link with multimode optical amplifier. *Proceedings ECOC Postdeadline* Paper PD1.1 (2019).

S16. M. Arikawa, T. Ishikawa, K. Hosokawa, S. Takahashi, Y. Ono, and T. Ito, Mitigation of fading caused by atmospheric turbulence with FMF coupling and maximum ratio combining used in 320-m free-space optical transmission of 10 Gb/s BPSK. *Proceedings ECOC* 1205–1207 (2016).

S17. D. Zheng, Y. Li, H. Zhou, Y. Bian, C. Yang, W. Li, J. Qiu, H. Guo, X. Hong, Y. Zuo, I. P. Giles, W. Tong, and J. Wu, Performance enhancement of free-space optical communications under atmospheric turbulence using modes diversity coherent receipt. *Opt. Express* **26**, 28879–28890 (2018).

S18. J. D. Deschênes, L. C. Sinclair, F. R. Giorgetta, W. C. Swann, E. Baumann, H. Bergeron, M. Cermak, I. Coddington, and N. R. Newbury, Synchronization of distant optical clocks at the femtosecond level. *Phys. Rev. X* **6**, 021016 (2016).